This is a preprint of the following article:
Shamsheer S. Chauhan and J. R. R. A. Martins. Tilt-wing eVTOL takeoff trajectory optimization. *Journal of Aircraft*, 2019.
The published article may differ from this preprint and is available at:
https://doi.org/10.2514/1.C035476.

Tilt-wing eVTOL takeoff trajectory optimization

Shamsheer S. Chauhan and Joaquim R. R. A. Martins
University of Michigan, Ann Arbor, MI, 48109

Abstract

Technological advances in areas such as battery technology, autonomous control, and ride-hailing services, combined with the scale-free nature of electric motors, have sparked significant interest in electric vertical takeoff and landing (eVTOL) aircraft for urban air mobility. In this work, we use simplified models for the aerodynamics, propulsion, propeller-wing flow interaction, and flight mechanics to carry out gradient-based optimization studies for the takeoff-to-cruise trajectory of a tandem tilt-wing eVTOL aircraft. We present results for optimizations with and without stall and acceleration constraints, with varying levels of flow augmentation from propellers, and find that the optimal takeoffs involve stalling the wings or flying near the stall angle of attack. However, we find that the energy penalty for avoiding stall is practically negligible. Additionally, we find that without acceleration constraints, the optimized trajectories involve rapidly transitioning to forward flight and accelerating, followed by climbing at roughly constant speed, and then accelerating to the required cruise speed. With an acceleration constraint for passenger comfort, the transition, climb, and acceleration phases are more gradual and less distinct. We also present results showing the impact of wing loading and available power on the optimized trajectories.

1 Introduction

The fundamentally different nature of electric motors, compared to combustion engines, allows developing unconventional aircraft configurations that would otherwise be impractical. This, combined with advances in battery technology, autonomous control, and ride-hailing services, makes large-scale urban air transportation seem more feasible than ever. This possibility of urban air transportation is currently receiving significant interest and a large number of different electric vertical takeoff and landing (eVTOL) aircraft are currently under development. A few examples of the companies currently developing passenger eVTOL aircraft are Airbus, Aurora Flight Sciences

(a Boeing subsidiary), EHang, Joby Aviation, Kitty Hawk, Lilium, and Volocopter. Most of the concepts under development can be categorized into a few major categories of aircraft type. Four of these major categories are multicopter (e.g., Volocopter 2X), lift+cruise (e.g., Kitty Hawk Cora), tilt-rotor (e.g., Joby S4), and tilt-wing (e.g., Airbus A^3 Vahana) [1].

An eVTOL aircraft currently being developed by Airbus A^3, called the Vahana, has a tandem tilt-wing configuration. This type of aircraft has tilting wings with propellers on them that allow the aircraft to takeoff and land vertically like a helicopter, but cruise like an airplane. This configuration is one of the many solutions that allow achieving both the takeoff and landing flexibility of helicopters, and the efficient forward flight of airplanes.

Tilt-wing aircraft first received serious attention in the 1950s and 1960s when a few companies including Boeing, Ling-Temco-Vought (LTV), Hiller, and Canadair developed flying prototype aircraft [2–8]. Several successful flight tests including transitions between vertical and horizontal flight were carried out [2–5, 7]. Flight-test summaries for the Boeing-Vertol VZ-2 [2] and Canadair CL-84 [5] report that flow separation and stalling of the wings provided piloting and operational challenges. Over 300 hours of flight testing was carried out for the LTV/Hiller/Ryan XC-142 to prove its suitability for operation [4]. Despite the extensive testing, due to several factors including challenges related to control and stability as well as mechanical complexity, interest was lost and these programs were eventually canceled. However, with modern control systems and the advantages of electric propulsion, modern tilt-wing concepts may be able to overcome these challenges. A significant amount of literature also exists from that period related to the design, performance, and control of tilt-wing aircraft [9–14]. More recent work has focused on the design and control of smaller tilt-wing unmanned aerial vehicles (UAVs) [15–19].

Transitioning from vertical to horizontal flight for a tilt-wing aircraft is a balancing act in which the propellers have to provide sufficient thrust to support the weight of the aircraft while also tilting with the wings to accelerate the aircraft to a speed and configuration where sufficient lift can be provided by the wings. This transition is an important consideration for the design of these types of aircraft. Separated flow over the wing, which is undesirable and avoided in conventional aircraft design, is an important concern during the transition for tilt-wing aircraft and may even be beneficial or unavoidable. Johnson et al. [1] briefly mention in their conference paper that their analysis for a tilt-wing eVTOL concept suggests that the wing is operating near or just beyond stall during transition. Based on testing for the NASA Greased Lightning GL-10 prototypes, it also seems possible that spending some time with the wing stalled may provide the most energy-efficient transition for a tilt-wing aircraft [19].

Stalling the wing during the transition process allows prioritizing acceleration and transitioning to the more efficient airplane configuration more quickly at the cost of some inefficient lift during early stages. However, it is not obvious whether this provides an overall benefit. Also, if it does, it is not obvious how much of a benefit it provides. One of our goals in this paper is to investigate this further for a tandem tilt-wing passenger eVTOL configuration based on the Airbus A^3 Vahana.

There is a lack of studies on the optimal takeoff trajectory for passenger tilt-wing

eVTOL aircraft. However, some related research has been carried out on transition optimization for tailsitter and flying-wing UAVs that take off vertically. Stone and Clarke [20] carried out numerical optimization studies for the takeoff maneuver of a 23–32 kg tailsitter twin-propeller wing-canard UAV with the objective of minimizing the time required to transition to forward flight and reach a specified altitude and speed. They limit the angles of attack in their optimization problem to prevent stalling the wing and conclude that it is possible for their UAV to transition without stalling the wing. They also note that as aircraft mass increases, the optimal takeoff maneuvers have increased angles of attack for greater portions of the maneuver. Another interesting observation from their results is that for larger aircraft masses, the optimal takeoff trajectory involves overshooting the target altitude and then descending to achieve it. In a later paper, Stone et al. [21] also discuss flight-test results for their UAV and note that during the vertical to forward-flight transition, the UAV lost altitude instead of gaining altitude as predicted by their simulations.

Kubo and Suzuki [22] numerically optimized the transitions between hover and forward flight for a 2 kg tailsitter UAV with a twin-propeller twin-boom wing-tail configuration. With the objective of minimizing transition time, and with stall constraints, they obtain an optimized transition from hover to forward flight without noticeable altitude change. They also note that high throttle settings during the transition help delay stall.

Maqsood and Go [23] numerically optimized transitions between hover and cruise for a small tailsitter tilt-wing UAV (tractor configuration without distributed propulsion) with the objective of minimizing the altitude variation during transition. They compare optimization results for the hover to forward-flight transition for a configuration with tilting wings and the same configuration with fixed wings. They note that the optimal transition with a tilting wing avoids stalling the wing, which reduces thrust requirements compared to a fixed-wing configuration.

Oosedo et al. [24] numerically optimized the hover to forward-flight transition for a 3.6 kg quadrotor tailsitter flying-wing UAV with the objective of minimizing the time required to transition. They compare optimization cases with and without constraints for maintaining altitude. They also compare their simulations to experimental flight tests. All four of the UAVs [20, 22–24] mentioned above are significantly different from the type of aircraft we are interested in, due to their configurations and sizes.

Two other related research efforts focus on the landing phase instead. Pradeep and Wei [25] optimized the speed profile and time spent in the cruise, deceleration-to-hover, hover, and descent phases given a fixed arrival time requirement for the Airbus A^3 Vahana configuration. However, they do not model or study the details of the transition from cruise to hover. Verling et al. [26] optimized the transition from cruise to hover for a 3 kg tail-sitter flying-wing UAV.

For all the optimization studies mentioned above, relatively low-order models are used for the multiple disciplines involved due to the complexity of the physics and the high computational cost of higher-order methods. For the aerodynamics, the approaches used by these studies include using a database with aerodynamic coefficients and derivatives from a panel method [20], using airfoil data with corrections [22], and interpolating wind-tunnel data [23, 24, 26]. For propulsion, these studies either use

momentum theory and variations of blade-element models [20, 22] or experimental data [24]. For the propeller-wing interaction, all of the above studies that consider it augment the flow over the wing using induced-velocity estimates based on momentum theory [22, 23, 26], except for Stone and Clarke [20] who connect a blade-element model to a panel-method model and account for both axial and tangential induced velocities [27]. For the flight dynamics, representing the aircraft using a three degrees-of-freedom (DOF) longitudinal model is the common approach [20, 22–24, 26].

To address the lack of literature on the optimal takeoff trajectory for passenger tilt-wing eVTOL aircraft, we present numerical optimization results for the takeoff-to-cruise phase of a tandem tilt-wing eVTOL configuration based on the Airbus A^3 Vahana. The optimization objective is to minimize the electrical energy required to reach a specified cruise altitude and speed. In this paper, we answer the following questions:

1. What does the optimal takeoff trajectory including transition and climb (to a cruise altitude and speed appropriate for air-taxi operations) look like?
2. Does the optimal trajectory involve stalling the wings and, if yes, how much of a benefit does it provide?
3. How does the augmented flow over the wings due to propellers affect the optimal trajectory and energy consumption?
4. How much electrical energy is required?
5. How does the wing loading affect the optimal trajectory?
6. How does the power-to-weight ratio affect the optimal trajectory?

We use simplified models, gradient-based optimization, and NASA's OpenMDAO framework [28, 29] (a Python-based open-source optimization framework) for the optimizations.

By "simplified" models we mean computationally inexpensive first-principles-based low-order models that capture the primary trends. To model the aerodynamics of the wings we use a combination of airfoil data, well-known relations from lifting-line theory, and the post-stall model developed by Tangler and Ostowari [30]. For the propulsion and propeller-wing interaction we use relations from momentum theory and blade-element theory. For the flight mechanics we use a simplified 2-DOF representation of the aircraft and the forward Euler method for time integration.

This paper is organized as follows. In Section 2 we describe the mathematical models used in this work. In Section 3 we describe the optimization problems. Finally, in Section 4, we present and discuss the optimization results.

2 Mathematical models

We use the simplified models for the aerodynamics, propulsion, propeller-wing interaction, and flight-mechanics disciplines as described in the rest of this section. As mentioned earlier, by "simplified" models we mean computationally inexpensive first-principles-based low-order models that capture the primary trends.

2.1 Aerodynamics

Figure 1 shows the side view of the aircraft configuration that we use for this work. It is a tandem tilt-wing configuration based on the Airbus A^3 Vahana. The configuration has two rectangular tilting wings, each with four propellers in front. The total wing planform area is $9\,\mathrm{m}^2$, an estimate based on online images of an Airbus A^3 Vahana full-scale flight-test prototype. For the configuration we model, we assume that the forward and rear wings are identical and have the same reference area for simplicity. However, note that the actual Airbus A^3 Vahana prototype has a smaller forward wing (approximately 20% smaller than the rear wing based on flight-test prototype images).

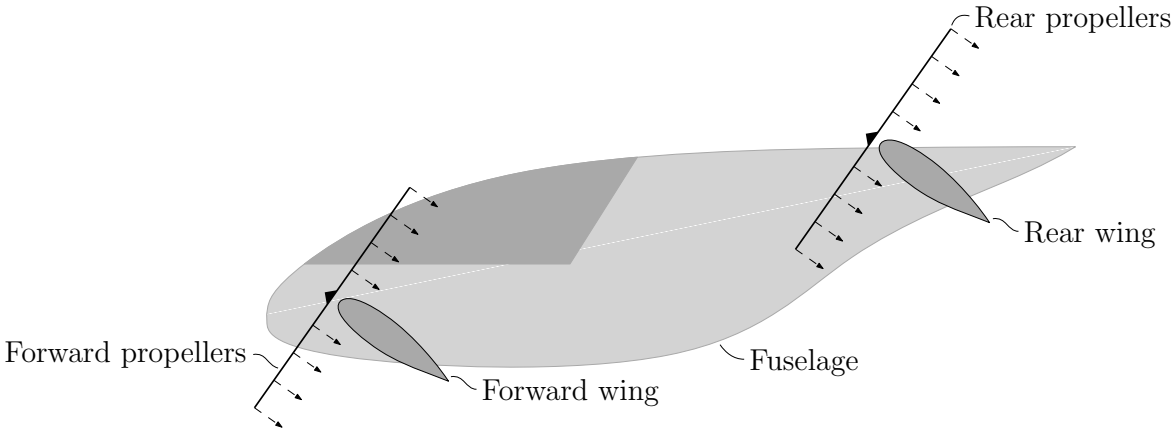

Figure 1: Side view of the VTOL configuration of interest. The configuration has two rectangular tilting wings.

Since separated-flow conditions need to be considered for the transition from vertical to horizontal flight, we require a model for the aerodynamics of the wings that also predicts the lift and drag beyond the linear-lift region. We use a model developed by Tangler and Ostowari [30] for non-rotating finite-length rectangular wings based on experimental data and the model of Viterna and Corrigan [31]. The post-stall lift coefficient is given by

$$C_{\mathrm{L}} = A_1 \sin 2\alpha + A_2 \frac{\cos^2 \alpha}{\sin \alpha}, \tag{1}$$

where

$$A_1 = \frac{C_1}{2}, \tag{2}$$

$$A_2 = \left(C_{\mathrm{L_s}} - C_1 \sin \alpha_{\mathrm{s}} \cos \alpha_{\mathrm{s}}\right) \frac{\sin \alpha_{\mathrm{s}}}{\cos^2 \alpha_{\mathrm{s}}}, \tag{3}$$

and

$$C_1 = 1.1 + 0.018AR. \tag{4}$$

Here, α is the wing angle of attack, α_{s} is the angle of attack at stall, $C_{\mathrm{L_s}}$ is the lift coefficient at stall, and AR is the wing aspect ratio. Before stall, the airfoil lift and drag are modified using the well-known finite-wing corrections from lifting-line theory for unswept wings in incompressible flow.

Between 27.5° and 90°, the drag coefficient is given by:

$$C_{\mathrm{D}} = B_1 \sin\alpha + B_2 \cos\alpha, \tag{5}$$

where

$$B_1 = C_{\mathrm{D}_{\max}}, \tag{6}$$

$$B_2 = \frac{C_{\mathrm{D_s}} - C_{\mathrm{D}_{\max}} \sin\alpha_{\mathrm{s}}}{\cos\alpha_{\mathrm{s}}}, \tag{7}$$

and

$$C_{\mathrm{D}_{\max}} = \frac{1.0 + 0.065AR}{0.9 + t/c}. \tag{8}$$

Here $C_{\mathrm{D_s}}$ is the drag coefficient at stall and t/c is the airfoil thickness-to-chord ratio. For the post-stall drag coefficient below 27.5°, the data points listed in Table 1 are used.

Table 1: Post-stall drag coefficient data points below 27.5° from Tangler and Ostowari [30]

α	C_{D}
16°	0.100
20°	0.175
25°	0.275
27.5°	0.363

Viterna and Corrigan [31] and Tangler and Ostowari [30] note that post-stall characteristics are relatively independent of airfoil geometry, which is why we do not see any input directly related to camber in the above equations. Tangler and Ostowari [30] also note that post-stall characteristics are relatively independent of the Reynolds number in the high-Reynolds range. Tangler and Ostowari [30] based their modifications to the Viterna and Corrigan [31] model on finite-length fixed-wing experimental data from Ostowari and Naik [32] who conducted tests at Reynolds numbers ranging from 0.25 million to 1 million. This also happens to be a reasonable Reynolds number range for the takeoff phase of the configuration we are looking at. The advantage of this model is that it provides reasonable predictions that can be evaluated at very little computational cost. In Appendix A, we have included plots that compare the above Tangler–Ostowari model to finite-wing experimental data from Ostowari and Naik [32] for NACA 4415 and NACA 4412 wings of different aspect ratio and with different Reynolds numbers.

For the airfoil used by the configuration of interest, we assume the NACA 0012 symmetric airfoil for simplicity. For the pre-stall aerodynamics, we refer to NACA 0012 experimental data from Critzos et al. [33] and Abbott and Von Doenhoff [34]. We estimated the lift-curve slope from the experimental data collected by Critzos et al.

[33] (smooth airfoil at $Re = 1.8 \cdot 10^6$) as $5.9\,\mathrm{rad}^{-1}$ and correct it using the following well-known correction for finite wings based on lifting-line theory:

$$a_{\text{wing}} = \frac{a_{\text{airfoil}}}{1 + \frac{a_{\text{airfoil}}}{\pi A R e}}, \tag{9}$$

where a_{wing} is the finite-wing lift-curve slope, a_{airfoil} is the airfoil lift-curve slope, and e is the span efficiency factor. We assume that the pre-stall lift curve is linear and that the stall angle of attack of the wing is 15°.

For each wing's parasite drag before stall, we use airfoil drag coefficient values from the NACA 0012 drag polar provided by Abbott and Von Doenhoff [34] (smooth airfoil at $Re = 3 \cdot 10^6$). The data points we use are listed in Table 5 in Appendix B under c_{d}. To obtain these c_{d} values from the drag polar, we first related α to the sectional lift coefficient, c_{l}. This was done using $c_{\text{l}} = \alpha \cdot a_{\text{airfoil}}$. Using this relation is not strictly correct because the sectional lift coefficient will vary across the wing. However, this gives a reasonable and conservative estimate. To these pre-stall parasite drag coefficients, we add induced drag using the well-known formula based on lifting-line theory,

$$C_{\text{D}_\text{i}} = \frac{C_{\text{L}}^2}{\pi A R e}, \tag{10}$$

to obtain the total drag of the wing before stall. Here C_{D_i} is the induced drag coefficient, C_{L} is the wing's lift coefficient, and for our configuration $AR = 8$ for each wing.

For simplicity, we compute the lift and drag of each wing in the tandem configuration as if they are independent and isolated wings. However, since we have a tandem configuration, we consider some interaction to determine the equivalent span efficiency, e, for each wing to avoid underpredicting drag. Based on the classical work of Munk and Prandtl [35], the induced drag of a biplane configuration with two identical wings generating the same amount of lift, $L_{\text{per wing}}$, is

$$D_{\text{induced}} = \frac{1}{\pi q}\left(2\frac{L_{\text{per wing}}^2}{b^2} + 2\sigma\frac{L_{\text{per wing}}^2}{b^2}\right), \tag{11}$$

where q is the freestream dynamic pressure, b is the span, and σ is a factor for the interference between the wings. This assumes that the two wings have elliptical lift distributions. For an equal-span tandem configuration with an effective gap-to-span ratio of 0.25, σ is approximately 0.4 [36].

For our configuration, we assume that with the effects of having a propeller at the wingtips, we can obtain a high span efficiency of approximately 0.95 for each wing in isolation. If we assume an effective gap-to-span ratio of 0.25 (i.e., $\sigma = 0.4$), and assume that Eq. (11) is valid for the assumed high span efficiency of 0.95, the induced drag for the configuration is

$$D_{\text{induced}} = 2\left(1.4\frac{L_{\text{per wing}}^2}{\pi q b^2 \cdot 0.95}\right) = 2\left(\frac{L_{\text{per wing}}^2}{\pi q b^2 \cdot 0.68}\right). \tag{12}$$

This means that when modeling the biplane as two isolated wings, the effective span efficiency, e, for each wing is approximately 0.68 (i.e., 0.95/1.4). We use this value of e

in Eq. (10) for our computations (computing the lift and drag of each wing as if they were isolated).

Since the Tangler–Ostowari model [30] described earlier only provides an analytic equation for the drag coefficient beyond 27.5°, we also desire an equation for the drag coefficient below this angle. To obtain an equation for the drag coefficient below 27.5°, we fit a quartic polynomial to the C_{D} values in Table 5 and Table 1 to obtain

$$C_{\mathrm{D}} = 0.008 + 1.107\alpha^2 + 1.792\alpha^4, \tag{13}$$

which is a least-squares fit where α is in radians. This curve and the data points are plotted in Fig. 16 in Appendix B.

The resulting lift and drag curves for each rectangular wing with $AR = 8$ using the Tangler–Ostowari [30] model are shown in Fig. 2. Since the curves shown in Fig. 2 have points at which the slopes are discontinuous, we use Kreisselmeier–Steinhauser (KS) functions [37] to make them C^1 continuous for gradient-based optimization. Figure 3 shows the regions of the lift and drag curves that are C^1 discontinuous and compares them to the curves from the KS functions that are used to smooth them.

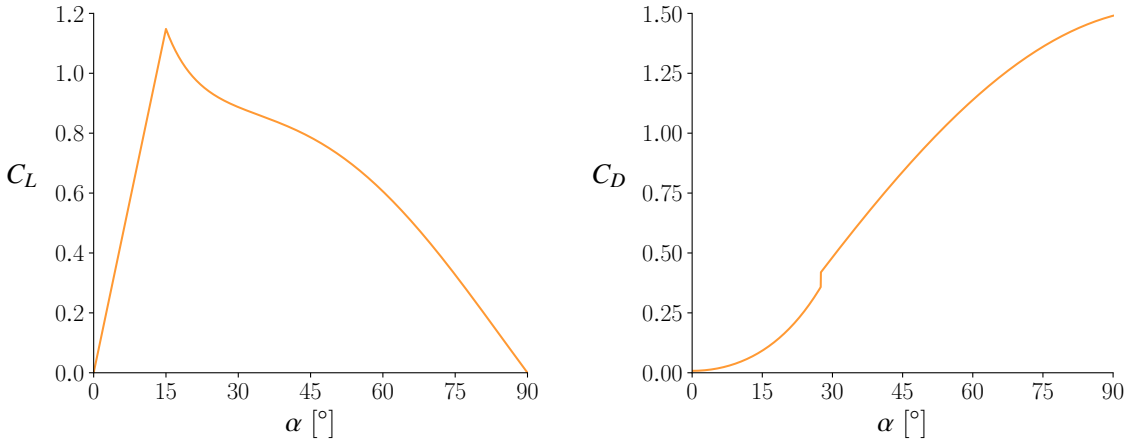

(a) Lift coefficient

(b) Drag coefficient

Figure 2: Finite-wing ($AR = 8$) coefficients of lift and drag using the Tangler–Ostowari model

We must also note that for low flight speeds at the beginning of takeoff, especially for the cases where there is no flow over the wings from the propellers, the errors of this model may be significant due to the different behavior of flow at low Reynolds numbers [38].

This approach for modeling the aerodynamics of the wings is similar in nature to the approach used by Kubo and Suzuki [22], who use airfoil data that includes post-stall angles (−180° to 180°). However, it is not clear how they correct the airfoil data for finite-wing effects. As mentioned in the introduction, the other approaches used in studies similar to this work include using a database with aerodynamic coefficients and derivatives from a panel method [20] and interpolating wind-tunnel data [23, 24, 26].

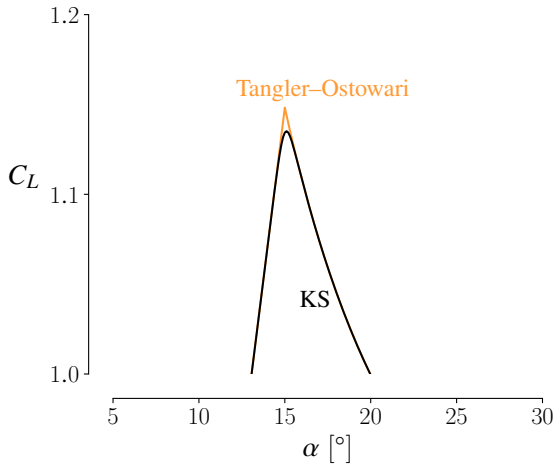

(a) Comparing the C^1-discontinuous part of the lift coefficient curve and the smooth KS function curve

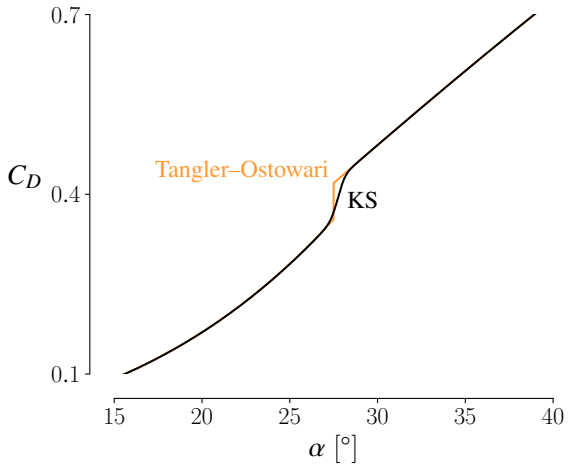

(b) Comparing the C^1-discontinuous part of the drag coefficient curve and the smooth KS function curve

Figure 3: Comparison of the C^1-discontinuous lift and drag coefficient curves to smooth curves obtained using KS functions

We have not come across the use of the Tangler–Ostowari [30] model in research related to airplane performance and design. However, this is not surprising because these relations are for the post-stall behavior of rectangular wings. Airplane performance and design usually does not require modeling post-stall behavior, and for the cases that do, the wings are usually not rectangular or in uniform freestream flow. The advantage of using the approach described here, over methods such as panel methods and RANS-based CFD, is that it provides reasonable predictions at very low cost due to the use of analytical equations. Additionally, obtaining accurate stall and post-stall predictions with higher-order methods such as panel methods and RANS-based CFD is a major challenge [39–44].

To the drag computed for the wings using the equations described above, we further add drag based on an assumed drag area of 0.35 for the fuselage and fixed landing gear, which is the value used in the open-source trade-studies code[1] shared by the Airbus A^3 Vahana team. We also assume that this coefficient for the fuselage and landing gear is independent of the freestream angle of attack and that the fuselage does not contribute any additional lift apart from the lift computed for the portions of the wing planforms that overlap with the fuselage.

As discussed earlier, we assume that both of the wings in our tandem configuration are identical. Apart from the interaction considered when computing the effective span efficiency for each wing, we assume that there is no interaction of flow between the two wings. We also assume that the two wings rotate identically, so this means that the angles of attack seen by the two wings are assumed to be identical, and so are the lift and drag that they generate. Additionally, we assume that the wings are

[1] https://github.com/VahanaOpenSource/vahanaTradeStudy[Accessed: Dec 2018]

located forward and aft of the center of gravity (CG) such that their moments are always balanced and ignore any fine-tuning required for trim and stability. In reality, even with symmetric airfoils and identical vertically offset wings located with their quarter-chords equidistant from the CG, the forces and moments on the wings will not be identical and the aircraft will not stay perfectly balanced due to several factors including upwash and downwash, propeller interactions, CG movement, and fuselage moments. However, we assume their effects to be small and also neglect the effects of any rotation caused by them on the forces on the aircraft.

2.2 Propulsion

To compute thrust from the propellers as a function of power, we use the following relation based on momentum theory:

$$P_{\text{disk}} = TV_{\infty\perp} + \kappa T \left(-\frac{V_{\infty\perp}}{2} + \sqrt{\frac{V_{\infty\perp}^2}{4} + \frac{T}{2\rho A_{\text{disk}}}} \right), \tag{14}$$

where P_{disk} is the power supplied to the propeller disk excluding profile power, T is the thrust, $V_{\infty\perp}$ is the component of the freestream velocity normal to the propeller disk, ρ is the air density, A_{disk} is the disk area of the propeller, and κ is a correction factor to account for induced-power losses related to non-uniform inflow, tip effects, and other simplifications made in momentum theory ($\kappa = 1$ for ideal power). We use power as a design variable in the optimization problems studied in this work and use the Newton–Raphson method to solve this nonlinear equation for thrust, T, with power as an input. The propeller radius assumed for our configuration is 0.75 m, an estimate based on online images of an Airbus A^3 Vahana full-scale flight-test prototype, which translates to a total disk area of 14.1 m^2 for eight propellers. For κ, we assume a value of 1.2.

Note that the equations of momentum theory are typically derived and used for propellers with purely axial inflow [13], which is not the case in general for a tilt-wing aircraft. Using the freestream velocity component normal to the propeller disk, as done here, satisfies the simplified control-volume analysis used to derive the equations. However, the sources of error in the predictions increase. Momentum theory requires several assumptions including assuming that the inflow and the propeller loading are radially and azimuthally uniform. For a propeller with purely axial inflow, the flow and loading are not radially uniform in reality, and with an angle of incidence to the freestream flow, they will not be azimuthally uniform either. Still, Eq. (14) provides idealized estimates for the power required for a given amount of thrust, which we roughly correct using the κ factor and profile-power estimates described later.

Glauert [45] derived another modified version of momentum theory for cases in which the freestream flow is not normal to the disk. Glauert's modified derivation is based on the observation that the induced velocity of a rotor in forward flight, when the freestream velocity component parallel to the rotor axis is small, corresponds more closely to the induced velocity of a wing than that of a typical propeller [45]. We do not use Glauert's modified version of momentum theory because we consider it to be

more appropriate for edgewise flight although it gives similar, but slightly higher (0 to 10%), thrust predictions for the combinations of angles, speeds, and powers that we are interested in.

To estimate the thrust and power of a propeller at moderate and high incidence as a function of advance ratio and blade pitch setting, de Young [46] provides semi-empirical relations for the ratios of thrust and power for a propeller at incidence to the thrust and power with zero incidence for an advance ratio corresponding to the freestream velocity component normal to the propeller. These relations, and the experimental data that they are informed by, show that as the angle between the propeller axis and the freestream velocity increases, the thrust and power both generally increase for a given advance ratio and blade pitch setting. For the range of angles and advance ratios that we expect, and with a rough range of blade pitch settings that we can expect for the configuration we are studying, our estimates using the equations from de Young [46] show that the thrust-to-power ratio for the propellers at incidence to the thrust-to-power ratio with zero incidence for an advance ratio corresponding to the freestream velocity component normal to the propellers remains close to 1 ($\sim$ 1.0 to 1.05). This gives us further confidence that the approach we use to estimate thrust as a function of power, which is based on the freestream velocity component normal to the propeller, provides reasonable trends.

For a rough estimate of profile power, we use

$$C_{\mathrm{P_p}} = \frac{\sigma C_{\mathrm{d_{0p}}}}{8}(1 + 4.6\mu^2), \tag{15}$$

which is a formula based on blade-element theory for a rotor in non-axial forward flight [13, 47]. Here, $C_{\mathrm{P_p}}$ is the coefficient of profile power defined as $C_{\mathrm{P_p}} = P_{\mathrm{p}}/(\rho A_{\mathrm{disk}} R^3 \Omega^3)$, where P_{p} is the profile power, R is the radius of the propeller, and Ω is the angular speed. Additionally, σ is the solidity, $C_{\mathrm{d_{0p}}}$ is a representative constant profile drag coefficient, and μ is defined as $V_{\infty\parallel}/(\Omega R)$ where $V_{\infty\parallel}$ is the component of the freestream velocity parallel to the disk. This provides a rough estimate for profile power that also has a dependence on the incidence angle of the propeller. For Ω, we assume that the propellers are variable-pitch propellers that operate at a constant angular speed corresponding to a tip speed of Mach 0.4 at hover for relatively low-noise operation, this gives a value of Ω =181 rad/s for $R = 0.75$ m. For the representative blade chord we use an estimate of 0.1 m based on Airbus A^3 Vahana flight-test prototype images, which translates to a solidity of 0.13 for each 3-blade propeller. For $C_{\mathrm{d_{0p}}}$ we assume a value of 0.012. The approach of using momentum theory and a profile-power formula to model the performance of a tilting propeller is described by McCormick [13] and compared with experimental data to show good agreement.

With electrical power as an input, we compute P_{disk} as

$$P_{\mathrm{disk}} = 0.9 P_{\mathrm{electrical}} - P_{\mathrm{p}}, \tag{16}$$

where $P_{\mathrm{electrical}}$ is the power from the batteries. We use the 0.9 factor to account for electrical and mechanical losses related to the batteries, electrical systems, and the motors. For the optimization problems, we limit the maximum electrical power

available to 311 kW. This is the electrical power, calculated using Eqs. (16) and (14), required to achieve a total thrust equal to 1.7 times the weight at hover (the 1.7 factor is taken from the Airbus A^3 Vahana design process blog[2]). We also assume that the axes of rotation of the propellers line up with the chord lines of the wings.

When the freestream flow is not normal to the propeller disks, the propellers will also generate forces normal to their axes. We estimate these normal forces using empirical formulas from de Young [46]. The normal force is calculated as

$$N = \frac{4.25\sigma_{\mathrm{e}} \sin(\beta + 8^\circ) f q_\perp A_{\mathrm{disk}}}{1 + 2\sigma_{\mathrm{e}}} \tan \alpha_{\mathrm{in}}, \tag{17}$$

where β is the blade pitch angle at $0.75R$, $q_\perp$ is the dynamic pressure based on the freestream velocity component normal to the propeller disk, A_{disk} is the propeller area, and α_{in} is the incidence angle. The other terms are computed as follows. The effective solidity, σ_{e} is

$$\sigma_{\mathrm{e}} = \frac{2Bc_{\mathrm{b}}}{3\pi R}, \tag{18}$$

where, B is the number of blades per propeller, c_{b} is the average chord length of the blades, and R is the propeller radius. The thrust factor, f, is

$$f = 1 + \frac{\sqrt{1 + T_{\mathrm{c}}} - 1}{2} + \frac{T_{\mathrm{c}}}{4(2 + T_{\mathrm{c}})}, \tag{19}$$

where, T_{c} is a thrust coefficient defined as $T_{\mathrm{c}} = T/(q_\perp A_{\mathrm{disk}})$ and T is the thrust. For rough values of β to use in Eq. (17), we assume that the blade angle changes linearly from 10° at a flight speed of 0 m/s to 35°at the cruise speed of 67 m/s (i.e., linearly with advance ratio with a fixed rotation speed). For most propeller aircraft, the incidence angles of the propellers during normal operation are small and the resulting normal forces are also small and can be neglected, especially during early performance studies. For some of our cases, the incidence angles will be relatively large during transition. However, since the flight speeds will be relatively low during transition, the normal forces generated will still be small in comparison to the thrust forces and weight of the aircraft.

As mentioned in the introduction, blade-element methods are commonly used to model the performance of propellers [20, 22, 48]. We use momentum theory instead of blade-element methods because it provides reasonable predictions and captures the major trends (e.g., the decrease in thrust with increase in flight speed) at very low computational cost. If we desired higher accuracy and wanted to take the geometry and pitch settings of specific blades and propellers into consideration, blade-element methods would be an option.

2.3 Propeller-wing interaction

Accurately modeling the interaction between a wing and the flow induced by propellers is a challenging undertaking and an area of active research due to its complexity [49–54]. In order to take this interaction into consideration in a simple manner, we once

[2] https://vahana.aero/vahana-design-process-part-ii-preparing-for-lift-off-a75b7ef6d583[Accessed: Dec 2018]

again turn to momentum theory. Based on momentum theory, the propeller increases the normal component of the freestream velocity in the streamtube to $V_{\infty\perp} + v_\mathrm{i}$ at the propeller disk and to $V_{\infty\perp} + 2v_\mathrm{i}$ at distances far downstream of the disk. The induced speed at the disk, v_i, is given by

$$v_\mathrm{i} = \left(-\frac{V_{\infty\perp}}{2} + \sqrt{\frac{V_{\infty\perp}^2}{4} + \frac{T}{2\rho A_\mathrm{disk}}} \right). \tag{20}$$

The induced speed far downstream of the propeller, $2v_\mathrm{i}$, gives us an upper bound for the effective increase in flow speed downstream of a propeller. In reality, since this model makes many simplifications, including neglecting viscous effects and assuming uniform flow, it is practically impossible for the effective flow speed seen by a wing behind a propeller to increase by this value. However, this gives us a range within which the increased effective speed seen by a wing will lie. To account for the propeller-wing flow interaction in our simulations, we increase the chordwise component of the freestream velocity for the entire wing by a range of factors, k_w, between 0 and 200%, multiplied by the induced speed at the disk, v_i.

According to Selig [48], when the aircraft speed is low and the propellers are highly loaded, the wake of the propeller is similar to a free jet and the wake speed within a few propeller diameters can be assumed to be the same as the speed at the disk (i.e., $k_\mathrm{w} \approx 100\%$). For higher speeds when the propellers are lightly loaded, the contraction of the streamtube occurs within a few disk diameters [48] and the additional speed of the wake will be between v_i and $2v_\mathrm{i}$ (i.e., $100\% < k_\mathrm{w} < 200\%$) within a few disk diameters.

For the wings of configurations like the Airbus A^3 Vahana, since the wake of the propellers does not completely and uniformly envelope the entire wing, and due to other simplifications made in the momentum theory, the effective k_w for the wing, especially at low speeds, is likely to be less than but close to 1. However, since this is difficult to predict accurately, we look at a wide range of k_w (0 to 200%) to study how it impacts the optimization results.

We neglect any interaction between the forward and rear propellers, any interaction between the wakes of the forward propellers and the rear wing, and any interaction between the forward wing and the streamtubes of the rear propellers. Due to the vertical separation of the wings, and because the wing angles for the takeoff phase will primarily lie between 0°and 90°to the horizontal, no significant flow interaction is expected.

This approach of augmenting the flow over the wings using the induced-velocity estimate from momentum theory with adjustment factors is common practice [22–24, 26, 48, 55]. However, one difference in our approach is that we consider a range of induced-velocity factors, k_w, instead of assuming a particular value or using a particular formula, such as the one for streamtube contraction provided by McCormick [13], to compute the value. This allows us to study how the flow augmentation impacts the optimization results.

2.4 Dynamics

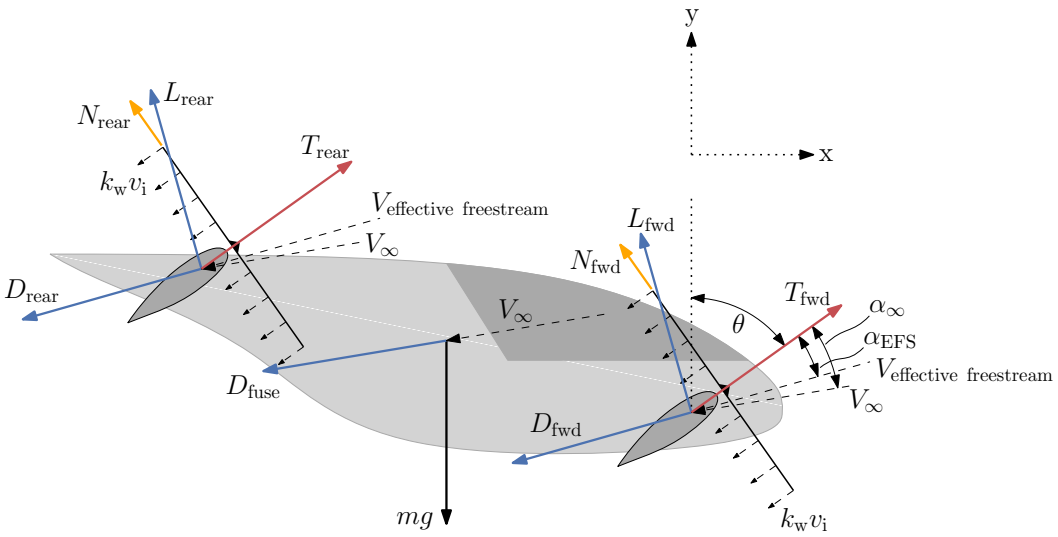

Figure 4: Angle definitions and forces on the aircraft

To simulate the trajectory of the aircraft, we use a 2-DOF representation and the forward Euler method. We solve for the aircraft's horizontal and vertical components of velocity as a function of time given the control variables, which are the wing-tilt angle and electrical power. The horizontal component of velocity at each time step is computed as

$$v_{\text{x}_{i+1}} = v_{\text{x}_i} + \frac{T\sin\theta - D_{\text{fuse}}\sin(\theta+\alpha_\infty) - D_{\text{wings}}\sin(\theta+\alpha_{\text{EFS}}) - L_{\text{wings}}\cos(\theta+\alpha_{\text{EFS}}) - N\cos\theta}{m}\Delta t, \quad (21)$$

where i is the index of the time step, Δt is the length of each time step, θ is the wing angle relative to the vertical, α_∞ is the freestream angle of attack, α_{EFS} is the effective freestream angle of attack seen by the wings due to the propellers, m is the mass of the aircraft, T is the total thrust, D_{fuse} is the drag of the fuselage, D_{wings} is the total drag of the two wings, L_{wings} is the total lift of the two wings, and N is the total normal force from the propellers. The angles and forces are illustrated in Fig. 4. As mentioned earlier, we assume that the two wings are identical, and rotate and behave identically. Similarly, the vertical component of velocity at each time step is computed as

$$v_{\text{y}_{i+1}} = v_{\text{y}_i} + \frac{T\cos\theta - D_{\text{fuse}}\cos(\theta+\alpha_\infty) - D_{\text{wings}}\cos(\theta+\alpha_{\text{EFS}}) + L_{\text{wings}}\sin(\theta+\alpha_{\text{EFS}}) + N\sin\theta - mg}{m}\Delta t, \quad (22)$$

where g is the acceleration due to gravity.

The time-step length, Δt, is computed as the flight time (which is a design variable in our optimization problem formulation) divided by 500. As we will see later, the flight times for the optimized takeoffs lie below 50 s, this translates to time steps less than 0.1 s. Based on step-size convergence studies, we found that this is a sufficiently small time-step range.

The common approach used in the related optimization studies cited in the introduction is to represent the aircraft using a 3-DOF model (two displacements in the

longitudinal plane and one pitch-angle) [20, 22–24, 26]. However, we take advantage of our tandem configuration and reduce the number of DOF to two. As discussed earlier in Section 2.1, we assume that the wings are located forward and aft of the CG, and rotate identically, such that their moments are always balanced (or at least that the effects of any imbalanced moments are negligible). We also ignore any fine-tuning that would be required in reality for trim and stability. Additionally, we assume that the pitching moments generated by the fuselage and propellers, and the reaction moments generated when the actuators rotate the wings are negligible, and neglect the effects of any rotation caused by these on the forces on the aircraft. This gives the simplified 2-DOF model (vertical and horizontal displacements only) described above.

3 Optimization problem formulation

Table 2 summarizes the baseline optimization problem formulation that we use. Table 3 lists additional constraints that are added for some of the cases. The objective is to minimize the electrical energy consumed to reach an altitude of 305 m and a cruise speed of 67 m/s. These altitude and cruise-speed specifications are taken from the mission requirements shared by Uber Elevate in 2018[3,4]. We also use an altitude constraint to ensure that the aircraft does not fall below an altitude of 0 m. The additional constraints are stall constraints to keep the effective freestream angle of attack of the wings between $-15°$ and $15°$ (our assumed stall angles of attack), an acceleration constraint for passenger comfort, and horizontal-displacement requirements for consistent energy comparisons. The acceleration and horizontal-displacement constraint values will be explained further in later sections. To avoid defining constraint functions for altitude, wing angle of attack, and acceleration at each time step, we use KS functions to aggregate [56, 57] the constraints. Therefore, instead of 501 constraint functions each (recall that 500 is the number of time steps) for the altitude, positive stall, and negative stall constraints, we have one function for each. Note that the KS functions provide conservative values for the quantities being constrained. This means that the constrained values will not lie exactly on the constraint limits when it is optimal to do so. However, we selected parameters for the KS functions to keep the level of conservativeness low, allowing the constrained values to approach the constraint limits closely which will be visible in the optimization results.

The design variables are the angle of the wings (same for both wings), the total electrical power (all propellers are identical and receive the same power), and the flight time. Since the wing angle and electrical power are continuous functions of time, we parameterize them using 4^{th}-order B-splines with 20 evenly spaced control points each (Appendix D includes comparisons of optimization results using 5 to 40 control points). The bounds for the wing-angle control points are $0°$and $135°$to the vertical, the bounds for the electrical-power control points are 1 kW and 311 kW, and the bounds for the flight time are 5 s and 60 s. The initial velocity is 0 m/s in the horizontal direction and

[3] https://www.uber.com/info/elevate/ecrm/[Accessed: Dec 2018]

[4] https://s3.amazonaws.com/uber-static/elevate/Summary+Mission+and+Requirements.pdf[Accessed: Dec 2018]

Table 2: Baseline optimization problem formulation

	Function/variable	Note	Quantity
minimize	electrical energy consumed		
with respect to	wing angle to vertical	B-spline parameterized using 20 control points	20
	electrical power	B-spline parameterized using 20 control points	20
	flight time		1
		Total design variables	**41**
subject to	final altitude $\geq 305\,\mathrm{m}$	Uber-specified cruise altitude	1
	final horizontal speed $= 67\,\mathrm{m/s}$	Uber-specified cruise speed	1
	altitude ≥ 0		1
		Total constraint functions	**3**

Table 3: Additional constraints used for some of the optimization cases

Function/variable	Note	Quantity
angle of attack $\leq 15^\circ$	Positive stall-angle constraint	1
angle of attack $\geq -15^\circ$	Negative stall-angle constraint	1
acceleration magnitude $\leq 0.3\,g$	Acceleration constraint	1
final horizontal displacement $= 900\,\mathrm{m}$	Horizontal-displacement requirement	1

$0.01\,\mathrm{m/s}$ in the vertical direction (a small initial speed so that the angle of attack is defined at the initial condition). The initial altitude is $0.01\,\mathrm{m}$ (a small positive value so that the altitude constraint is not violated by the initial condition). These initial speeds and altitude can be interpreted either as starting from rest on the ground or starting from rest in a hover state at some baseline altitude.

We use the OpenMDAO optimization framework [28, 29] (version 2.6.0) and the SNOPT [58] gradient-based optimizer (version 7.2-5) to solve the optimization problems. We set the major optimality and major feasibility tolerances of SNOPT to 10^{-8}. Due to the low computational cost of the models and the relatively small number of design variables, we compute the gradients using the complex-step method [59]. The complex-step method provides the implementation ease and flexibility of finite-difference methods, but without the concerns related to step size and accuracy. However, as is the case for finite-difference methods, the computational cost of using the complex-step method scales poorly with the number of design variables. If we were using a very large number of design variables or computationally expensive models, this method for computing gradients would be very limiting. Since we are using computationally inexpensive models for this study, this is not an issue. Table 4 contains the aircraft specifications used for these optimizations. The scripts used to run the optimization problems are publicly available[5]. Each optimization problem takes on the order of minutes to solve on a desktop computer.

[5] https://bitbucket.org/shamsheersc19/tilt_wing_evtol_takeoff

Table 4: Parameters and specifications for the aircraft under consideration. These values are estimates based on the Airbus A^3 Vahana.

Specification	Value	Note
Takeoff mass, m	725 kg	
Total wing planform area, S_{ref}	9.0 m^2	4.5 m^2 for each wing
Wing span, b	6 m	Same for both wings
Propeller radius, R	0.75 m	Same for all propellers
Total number of propellers	8	
Number of blades per propeller, B	3	Same for all propellers
Representative blade chord, c_{b}	0.1 m	Same for all propellers
Maximum electrical power, P_{max}	311.0 kW	Power for $T = 1.7\,mg$ at hover

4 Optimization results

Section 4.1 presents optimization results without acceleration constraints or horizontal-displacement requirements to show what the optimized trajectories are when the optimizer is given the most freedom. After that, Section 4.2 presents optimization results with an acceleration constraint and a horizontal-displacement requirement. Finally, Sections 4.3 and 4.4 present optimization results with varying wing loading and power-to-weight ratio.

4.1 Results without acceleration constraints or horizontal-displacement requirements

4.1.1 Results without stall constraints

Figure 5 shows optimization results without stall constraints for the first set of optimization problems, which does not have acceleration constraints or horizontal-displacement requirements. The first row of subplots in Fig. 5 shows the wing-angle and electrical-power design variables (our control variables). The rest of the subplots in Fig. 5 show the state variables (vertical and horizontal displacements, wing angle of attack, speed, wing lift and drag, total thrust, and acceleration magnitude). The same optimization problem is solved for six different values of the propeller-induced velocity factor ($k_{\text{w}} =$ 0%, 25%, 50%, 75%, 100%, and 200%). A value of 0% corresponds to no flow augmentation from the propellers, and 200% is a conservative and likely unattainable upper limit for the effective flow augmentation. As discussed in Section 2.3, we expect the effective k_{w} to be less than 100% for the type of configuration we are studying.

In Fig. 5, from the subplot showing the wing angle of attack as a function of time, we see that for $k_{\text{w}} \leq 25\%$, the optimal trajectory involves transitioning to forward flight with the wings stalled during the first few seconds. For higher k_{w}, the optimizer does not choose to stall the wings. From the subplot showing the wing angle relative to the vertical, we see that the wing angle first increases during the initial transition phase, then decreases to around 37° to 40° during the climb phase, and finally increases again for level flight. The angle range of 37° to 40° allows the aircraft to climb at vertical

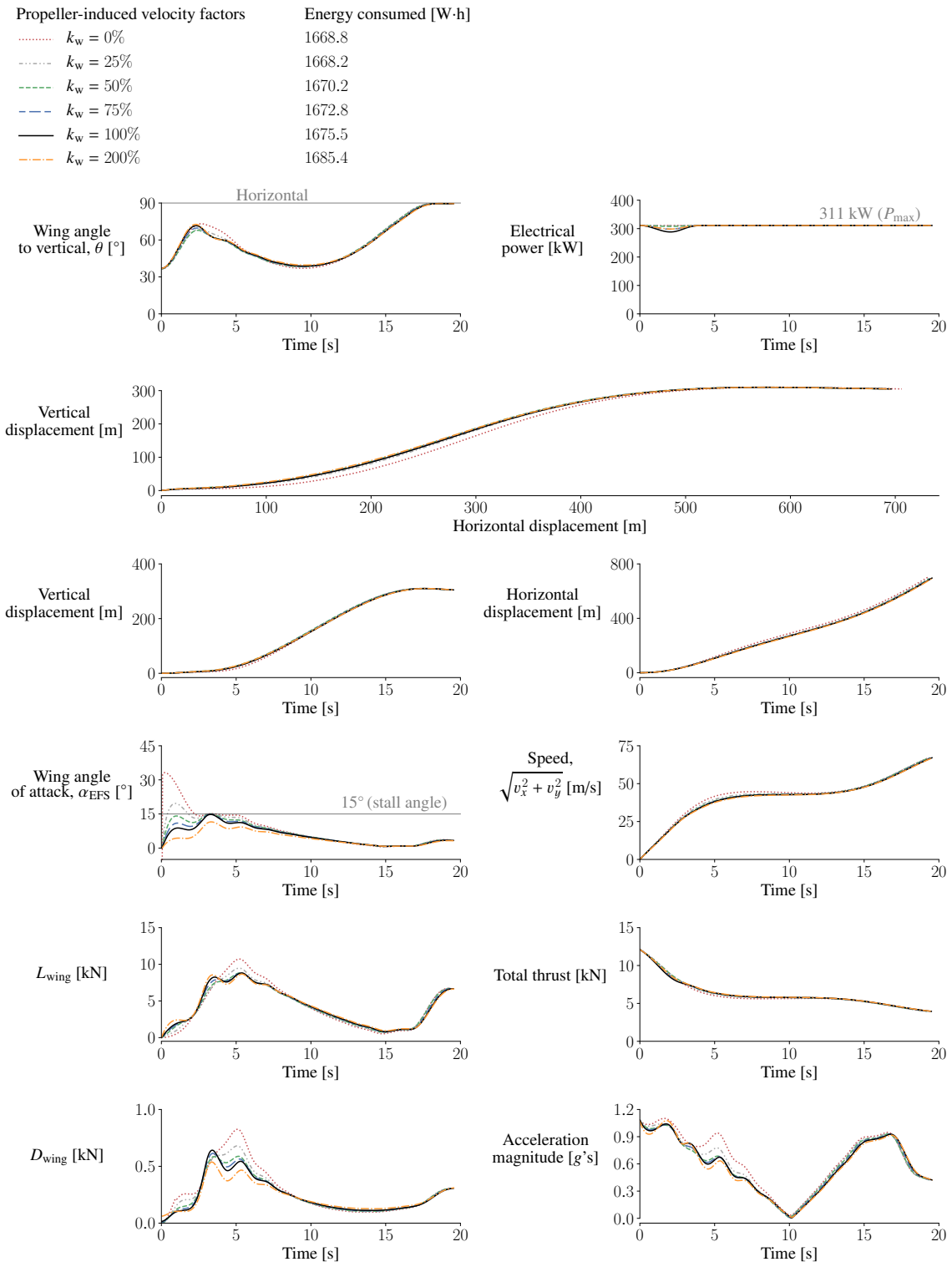

Figure 5: Results without stall constraints for the optimization problem set that does not have acceleration constraints or horizontal-displacement requirements

speeds near the best rate of climb for this aircraft (31 m/s). It is also interesting to note that the entire takeoff is carried out at or almost at maximum power for all k_w values.

From the displacement and speed subplots, we see that the optimized trajectories involve first transitioning rapidly to forward flight and accelerating, followed by climbing at roughly constant speed, and then finally accelerating to the required cruise speed. We also see that the optimal trajectories involve overshooting the required cruise altitude by a small margin and then descending while accelerating to the required cruise speed. These climb and acceleration features have been seen before in trajectory-optimization literature [60, 61].

The electrical energy consumption values listed in Fig. 5 show that the differences in energy consumed with or without the flow augmentation from propellers are practically negligible. Note that the horizontal distances covered in these results are different for the different k_w values and the differences would have to be made up in cruise. However, the maximum difference is 15 m which also corresponds to a practically negligible amount of energy difference.

4.1.2 Results with stall constraints

Fig. 6 shows results with stall constraints ($-15^\circ \leq$ angle of attack $\leq 15^\circ$) for the first set of optimization problems, which does not have acceleration constraints or horizontal-displacement requirements. The optimized trajectories are very similar to the optimized trajectories for the cases without stall constraints. The main difference is smaller wing angles relative to the vertical, for the cases with low flow augmentation from the propellers ($k_w \leq 25\%$), during the initial transition phase to keep the flow attached.

Figure 17 in Appendix C provides a closer view of the initial transition phase of the trajectories shown in Figs. 5 and 6. With low flow augmentation and with stall constraints, the optimal trajectories involve gaining more altitude and transitioning more gradually to avoid stalling the wings.

Once again, Fig. 6 shows that the energy consumption differences with or without the flow augmentation from propellers are practically negligible. Additionally, by comparing the energy values listed in Figs. 5 and 6, we see that the energy penalty to avoid stalling the wings is also practically negligible. Note again that for these cases the horizontal distances covered are slightly different, by a maximum of 27 m, which also corresponds to a practically negligible cruise energy difference. We add horizontal-displacement requirements for more consistent energy comparisons to the optimization problems discussed in the following sections.

The acceleration subplots in Figs. 5 and 6 show that the accelerations reach $1\,g$ in magnitude. These may be acceptable for applications such as package transportation or autonomous relocation of the aircraft, but would be uncomfortable for passengers. For the sets of optimization problems discussed in the following sections, we also add acceleration constraints for passenger comfort.

Figures 5 and 6 also show oscillations in the angle-of-attack, lift, and drag subplots, as well as some less obvious fluctuations in the wing-angle and thrust subplots, espe-

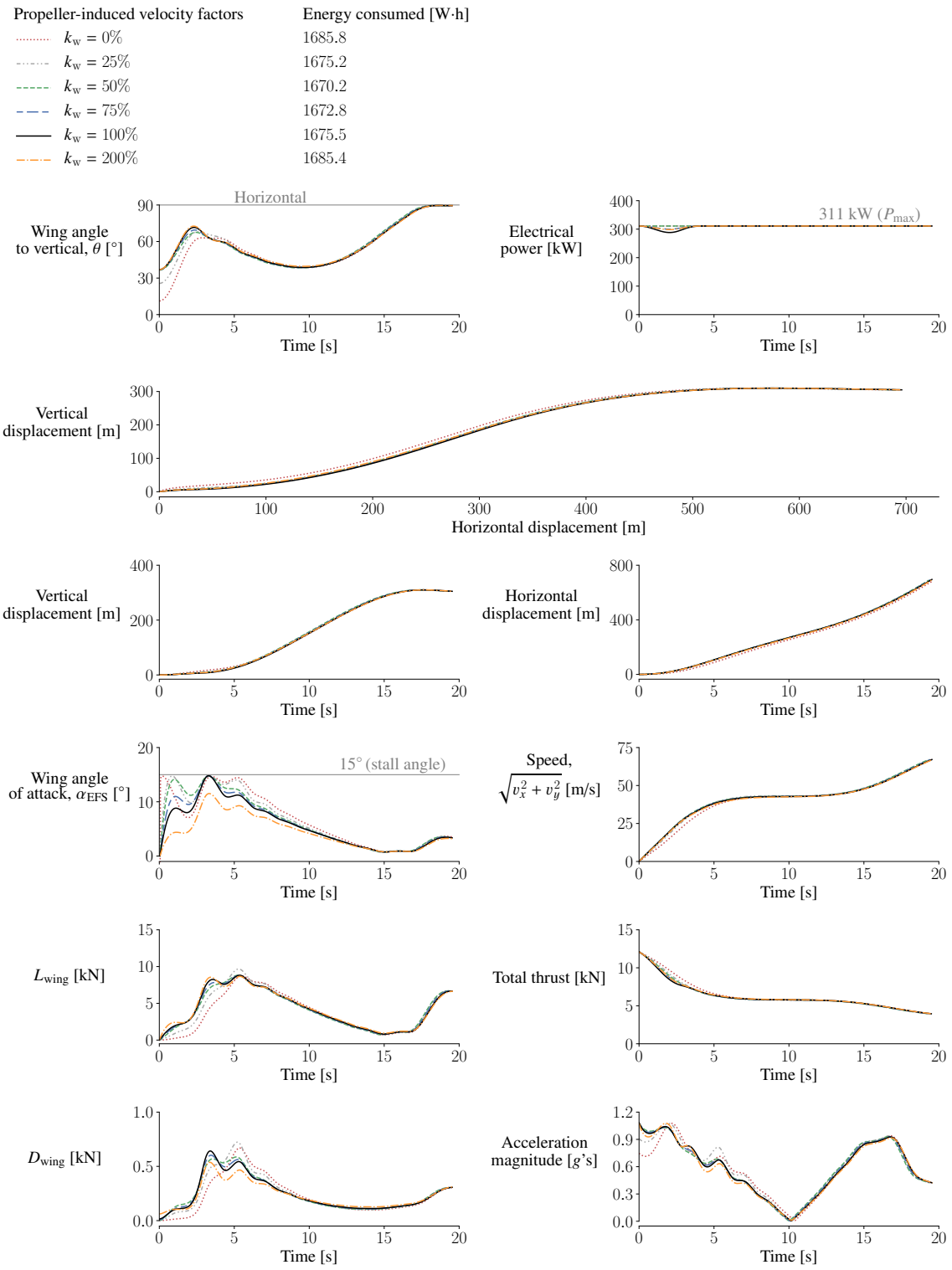

Figure 6: Results with stall constraints for the optimization problem set that does not have acceleration constraints or horizontal-displacement requirements

cially during the first ten seconds. The wing angle affects all the disciplines we model and therefore the exact tradeoffs being made here are not obvious. Changing the wing angle changes the component of the freestream velocity normal to the propeller disks, which for a given power changes the thrust, the induced velocities, and the propulsive efficiency. Changing the wing angle also changes the direction of the thrust vector which, along with the change in thrust magnitude, changes the acceleration and velocity of the aircraft, and also changes how much work is being done against gravity and to increase kinetic energy, and how much is being done against drag. Additionally, changing the wing angle, along with the resulting changes to the freestream velocity and induced velocities, also changes the angle of attack of the wings and the resulting forces which impact the aerodynamic performance. The magnitudes and relative sensitivities of these quantities to the wing angle are all different and also change with the evolving flight conditions, making it challenging to isolate benefits and explain the fluctuations and oscillations. However, since we are minimizing energy consumption, the problem boils down to maximizing total efficiency while satisfying the mission requirements. In Fig. 7, we plot propulsive efficiency and total efficiency as a function of time for the optimization results corresponding to Fig. 6. We define the propulsive efficiency as

$$\eta_{\text{prop}} = \frac{TV_{\infty\perp}}{P_{\text{electrical}}}, \tag{23}$$

and the total efficiency as

$$\eta_{\text{total}} = \frac{mgy + 0.5m(v_{\text{x}}^2 + v_{\text{y}}^2)}{\int P_{\text{electrical}}\,\mathrm{d}t}, \tag{24}$$

where y is the vertical displacement. The total efficiency is the ratio of the potential and kinetic energy to the electrical energy consumed. We do not see any significant fluctuations in the propulsive efficiency and the total efficiency curves. Additionally, the comparison of optimization results with different numbers of control points in Fig. 18 in Appendix D shows that the design space is relatively flat because even with smoother and significantly different control inputs and state variables when the number of control points is low, the differences in energy consumption are small (1% between the energy consumptions with 5 control points and 40 control points). Note that these optimization problems have been converged very tightly and the energy consumption decreases by only $\sim 10^{-5}\%$ or less over the last three orders of convergence of the optimality criterion, and therefore the oscillations are not a result of a lack of convergence. Based on this, we attribute the oscillations to a combination of the design freedom provided by the B-spline parameterization and the optimizer taking advantage of subtle tradeoffs and small benefits in the design space.

4.2 Results with an acceleration constraint and a horizontal-displacement requirement

Now we present optimization results with an acceleration constraint and a horizontal-displacement requirement. During takeoff, the longitudinal acceleration of commercial

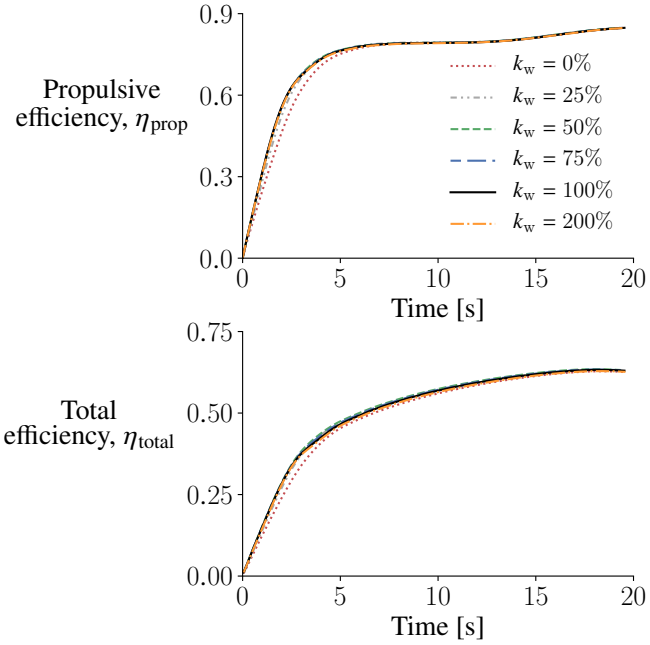

Figure 7: Propulsive and total efficiency as a function of time for the cases shown in Fig. 6

airplanes can reach up to $0.5\,g$ without significant discomfort for passengers [62]. Based on this we add a constraint to limit the magnitude of the accelerations to below $0.3\,g$ for passenger comfort. As discussed in Section 4.1, the different cases with and without stall constraints and with different k_w values had small differences in their final horizontal displacements and these differences would have to be made up in cruise. For more consistent comparisons, we add the requirement that the final horizontal displacement must be 900 m. First we ran the optimizations with the acceleration constraint, but without a horizontal-displacement requirement, and found that the final horizontal displacements ranged between 829 m and 869 m. Therefore we set the horizontal-displacement requirement to 900 m, a value greater than the above horizontal displacements.

4.2.1 Results without stall constraints

Figure 8 shows optimization results without stall constraints for the second set of optimization problems, which has the acceleration limit of $0.3\,g$ and the horizontal-displacement requirement of 900 m. The takeoffs are no longer carried out at maximum power and the wing angle now has a gradual increase instead of a rapid increase and decrease as seen in Fig. 5. With $k_w = 0$, the flow over the wing remains separated for the first 7 s, and for all other k_w values except 200%, the wings operate slightly beyond the stall angle of attack for a few seconds. The trajectories show greater gain in altitude during the initial phase compared to our previous set of results without the acceleration constraint. We also no longer see distinct acceleration and climb phases

as we did in the previous set of results.

The optimized trajectories now also have more noticeable differences between them for the different levels of flow augmentation. With lower levels of flow augmentation, the optimized trajectories involve taking off with smaller wing angles to the vertical and gaining more altitude during the initial takeoff phase. However, once again we find that the energy consumption differences are practically negligible for the different k_{w} values.

For a direct comparison to energy consumed without an acceleration constraint, energy consumption values are included in Table 6 in Appendix E for optimization cases without the acceleration constraint but with the horizontal-displacement requirement of 900 m. Without the acceleration constraint, the energy consumption is 9% lower on average.

4.2.2 Results with stall constraints

Figure 9 shows optimization results with stall constraints for the second set of optimization problems, which has the acceleration limit of $0.3\,g$ and the horizontal-displacement requirement of 900 m. Once again, we find that the energy consumption differences are practically negligible for the different k_{w} values and that the energy penalty to avoid stalling the wings is practically negligible as well.

To put the energy consumption values for the takeoff-to-cruise phase into perspective, we can estimate how much battery mass the electrical energy consumption translates to. The optimized takeoff-to-cruise energy consumption values for the cases with acceleration and horizontal-displacement requirements discussed so far range between 1862 Wh and 1875 Wh. With a cell-level specific energy of 200 Wh/kg (roughly the specific-energy value of the cells in today's high-end production electric vehicles) this translates to 9.5 kg of battery. Considering packaging, thermal management, and depth of discharge limitations, the installed-battery specific energy at current technology levels is likely to be closer to 100 Wh/kg [1], which translates to a battery weight of approximately 19 kg.

To further put the optimization results into perspective, we compare the energy consumption of the optimized profiles presented so far to a simpler, primarily hand-tuned, and somewhat more conventional climb in which the aircraft takes off, climbs at the wing angle for best rate of climb (θ_{RCmax}), and then accelerates to the required cruise speed. The simpler trajectory that we use has four phases. In the first phase, the aircraft takes off with the wing angle, θ, increasing from vertical to 35° and the power increasing from $70\%P_{\mathrm{max}}$ to $90\%P_{\mathrm{max}}$ over the first 10 s. In the second phase, the aircraft climbs to 250 m at maximum power with the wing angle set at 35°, which is θ_{RCmax} for our configuration. In the third phase, the aircraft transitions to horizontal flight by increasing the wing angle to 80° and reducing the power to $20\%P_{\mathrm{max}}$ over 10 s. Finally, in the fourth phase, the aircraft accelerates to the required cruise speed and satisfies the altitude and horizontal-displacement requirements. This simpler trajectory avoids stalling the wings and the phases have maximum accelerations in the 0.3 to $0.4\,g$ range. On average, this simpler strategy requires 5% more electrical energy than the optimized trajectories (the differences are 5% or 6% depending on the k_{w} value).

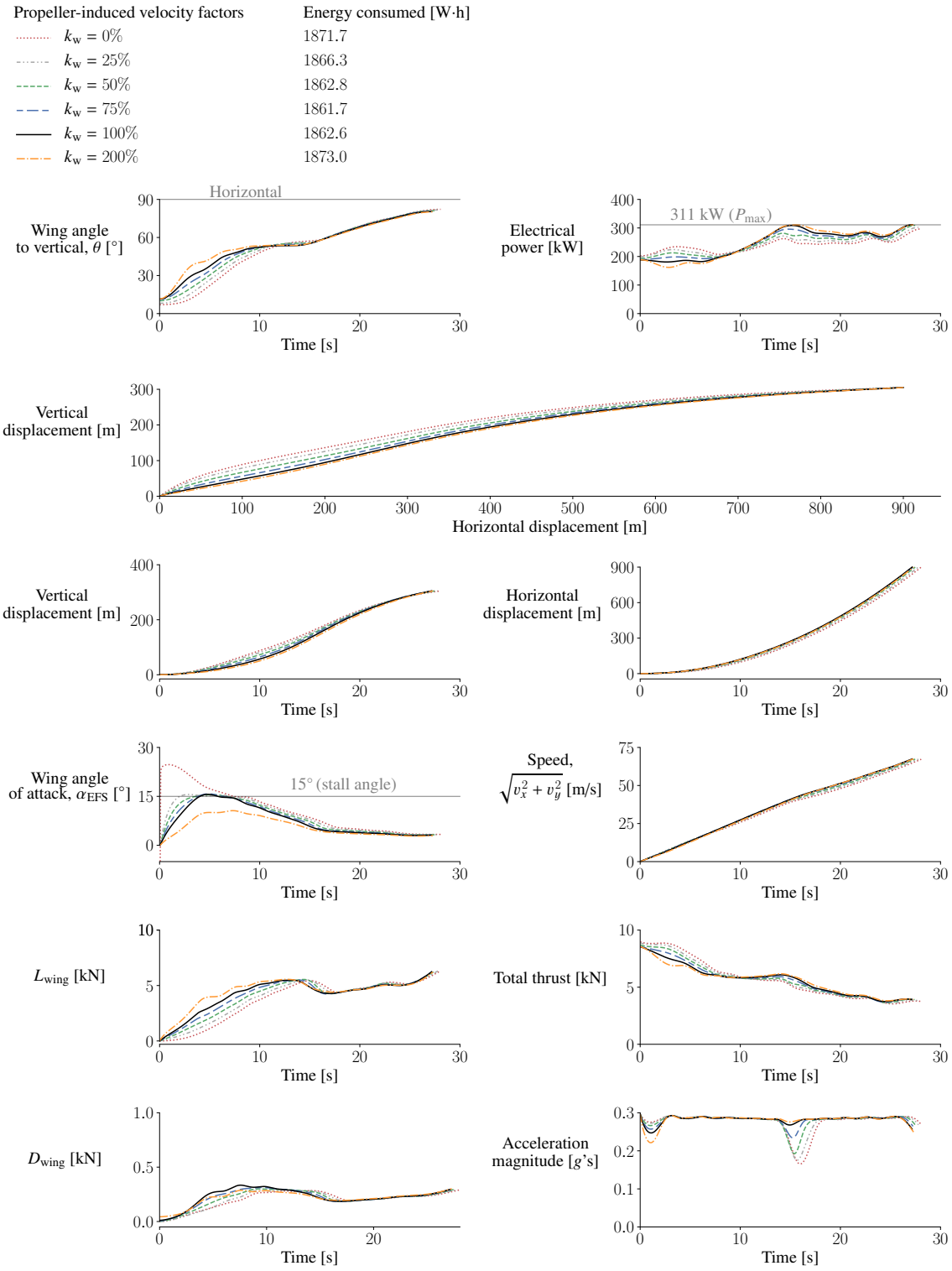

Figure 8: Results without stall constraints for the optimization problem set that has the acceleration limit of 0.3 g and the horizontal-displacement requirement of 900 m

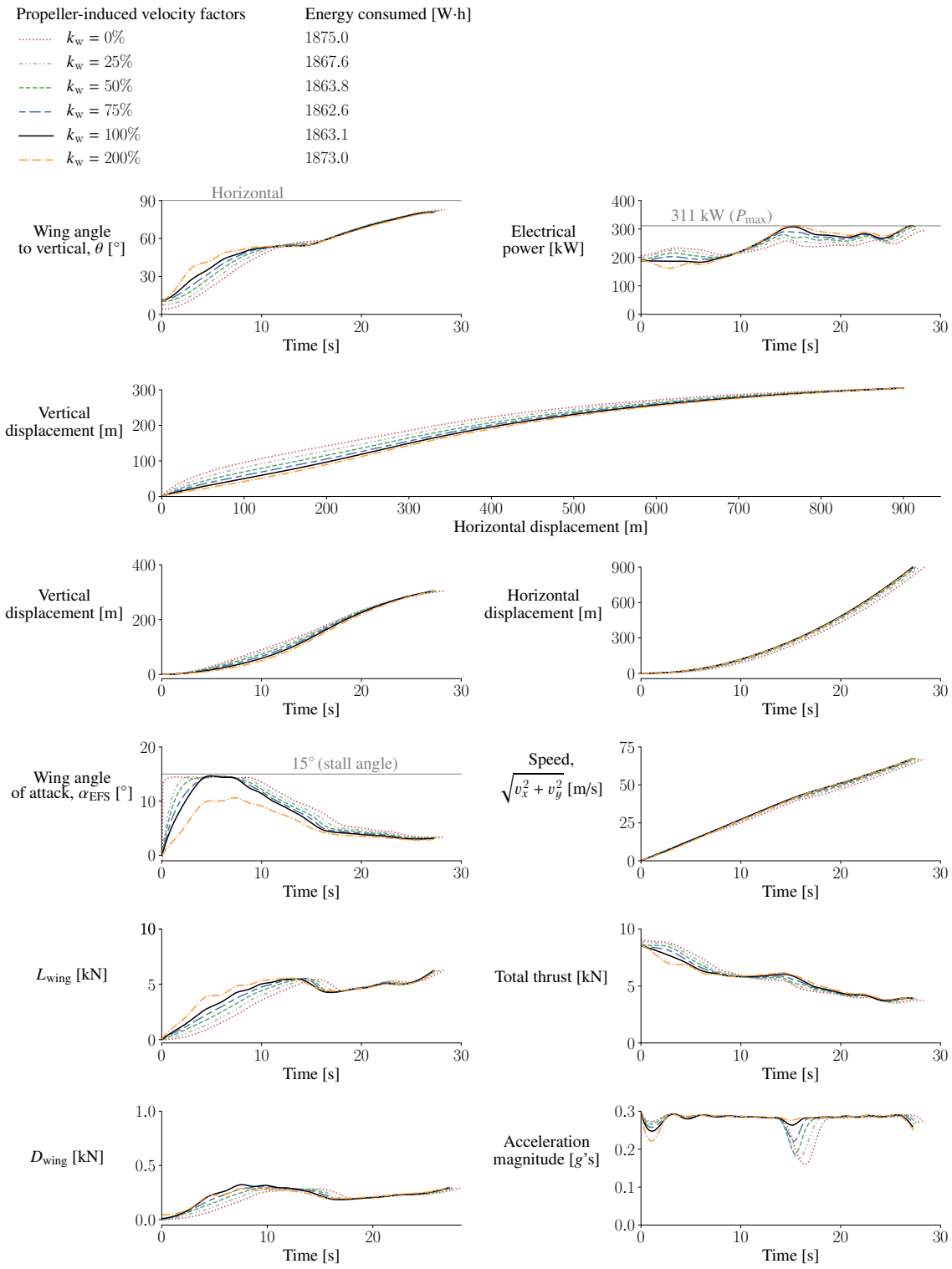

Figure 9: Results with stall constraints for the optimization problem set that has the acceleration limit of 0.3 g and the horizontal-displacement requirement of 900 m

In Appendix D, Figs. 18 and 19 show comparisons of optimization results with different numbers of B-spline control points (5, 10, 20, and 40 control points). The different numbers of control points provide varying levels of control on the design variables (our control variables); a larger number allows more rapid and frequent changes to the control variables. From Fig. 19 we see that with 10, 20, and 40 control points, the same trends are obtained and the differences in the energy consumption values are within 1%.

There is also the question of whether multiple local minima exist for these optimization problems. We solved the above optimization problems with over 50 different initial guesses for the wing-angle and electrical-power design variables (including constant, monotonically increasing, monotonically decreasing, and random values for the control points), as well as different initial guesses for the flight-time design variable, and did not find multiple local minima. Although this does not disprove the existence of other minima, it indicates that their existence is unlikely.

4.3 Results with higher wing loading

Since the results discussed so far are for an aircraft with a predetermined total wing planform area, it is also worth investigating what happens to the results when the wing size is different. We redo the optimizations that have the acceleration limit of $0.3\,g$ and the horizontal-displacement requirement of 900 m, with smaller wings (80%, 60%, and 40% of the baseline wing reference area, S_{ref}, with the span kept constant) to see what happens to the results. Note that we do not change the weight of the aircraft for these optimization cases. Figures 10 and 11 show optimization results with stall constraints for $k_{\text{w}} = 0\%$ and $k_{\text{w}} = 100\%$, respectively. We observe larger angles of attack with smaller wings, and also that it is still possible to avoid stall with significantly smaller wings. We have omitted plots for results without stall constraints; the main difference being angles of attack up to 25° in the first 7 s for $k_{\text{w}} = 0$ as seen in Fig. 8. When we compare the electrical energy consumed with the different planform areas, we see that the differences are small. This indicates that when designing the wings of a tilt-wing aircraft for urban mobility, factors such as avoiding flow separation during the takeoff phase and maximizing cruise efficiency should take precedence over considerations such as the energy consumed during the takeoff phase.

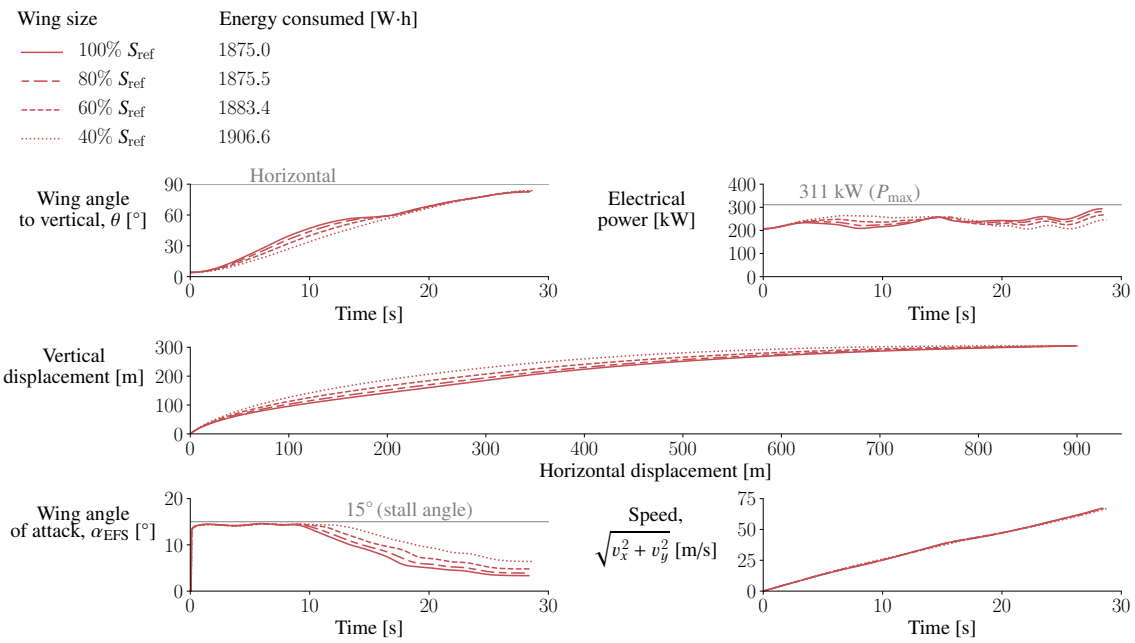

Figure 10: Results with different wing sizes for the optimization problem that includes the stall constraints, the 0.3 g acceleration limit, and the 900 m horizontal-displacement requirement ($k_w = 0$)

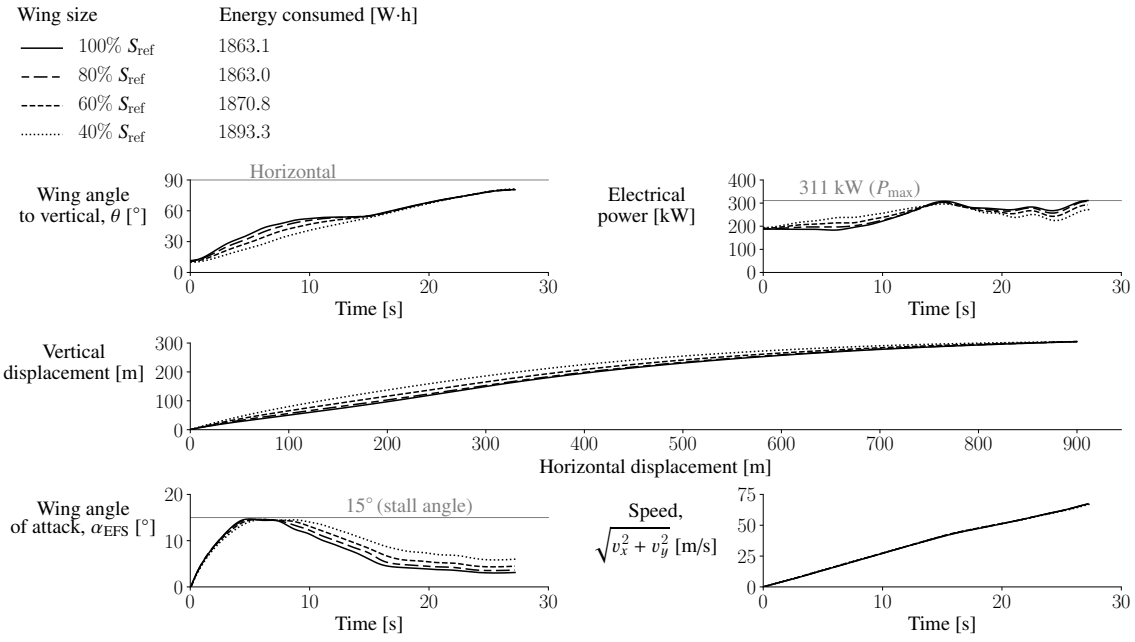

Figure 11: Results with different wing sizes for the optimization problem that includes the stall constraints, the 0.3 g acceleration limit, and the 900 m horizontal-displacement requirement ($k_w = 100\%$)

4.4 Results with lower power-to-weight ratios

Next, we also investigate what happens to the optimization results when the maximum power available decreases. We redo the optimizations that have the acceleration limit of $0.3\,g$ and the horizontal-displacement requirement of 900 m, with lower values for the upper bound of the electrical-power control variables (60%, 70%, and 80% of the baseline upper limit, $P_{\max}$). These maximum-power values correspond to thrust-to-weight ratios at hover equal to 1.19, 1.33, and 1.46 ($P_{\max}$ corresponds to 1.7). Note that we do not change the weight of the aircraft for these optimization cases.

Figures 12 and 13 show optimization results without stall constraints for $k_{\mathrm{w}} = 0\%$ and $k_{\mathrm{w}} = 100\%$, respectively. The takeoffs for the lower-power cases (60% $P_{\max}$ and 70% $P_{\max}$) are carried out almost completely at maximum power. With the available power limited to 60% $P_{\max}$ and 70% $P_{\max}$, we also see purely vertical flight phases in the optimized trajectories, something not seen in the other optimization results in this paper. These results also show that, up to a certain level due to the acceleration constraint, with more power available, less time and less electrical energy are required to reach the specified cruise altitude and speed. The lowest-power cases consume approximately 30% more electrical energy than the highest-power cases.

With stall constraints, the optimizer indicated that the optimization problems were infeasible with $k_{\mathrm{w}} \leq 50\%$ for 60% $P_{\max}$ and with $k_{\mathrm{w}} \leq 25\%$ for 70% $P_{\max}$. This shows that with low available power and low levels of flow augmentation, stalling the wings during takeoff can be unavoidable.

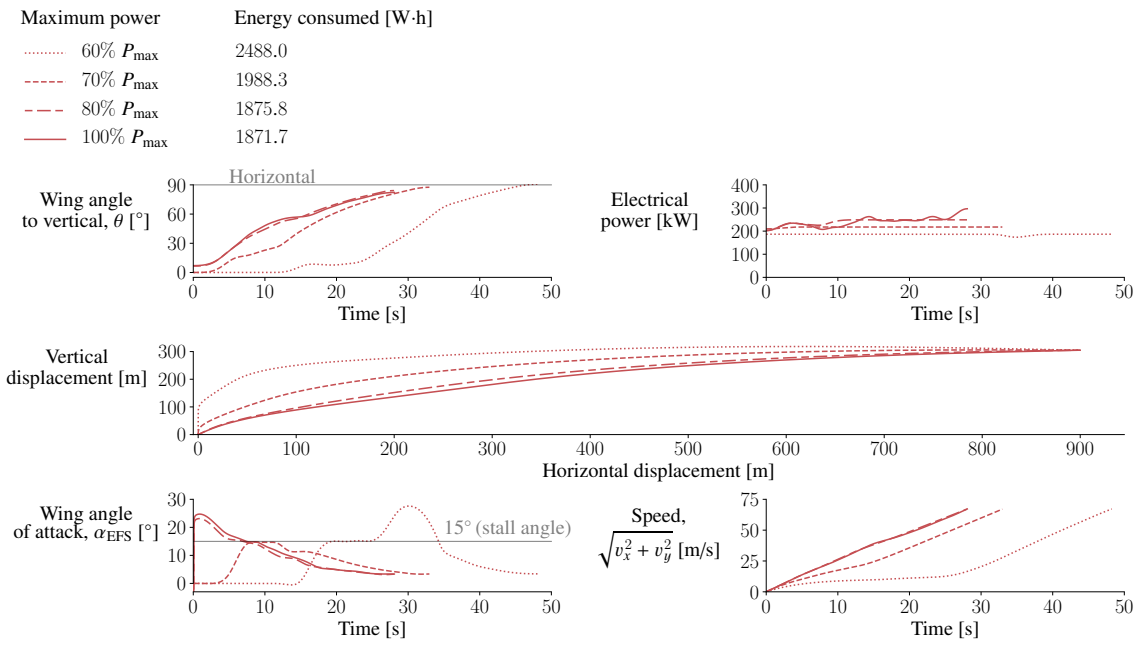

Figure 12: Results with varying maximum power for the optimization problem that includes the $0.3\,g$ acceleration limit and the 900 m horizontal-displacement requirement (no stall constraints, $k_{\mathrm{w}} = 0$)

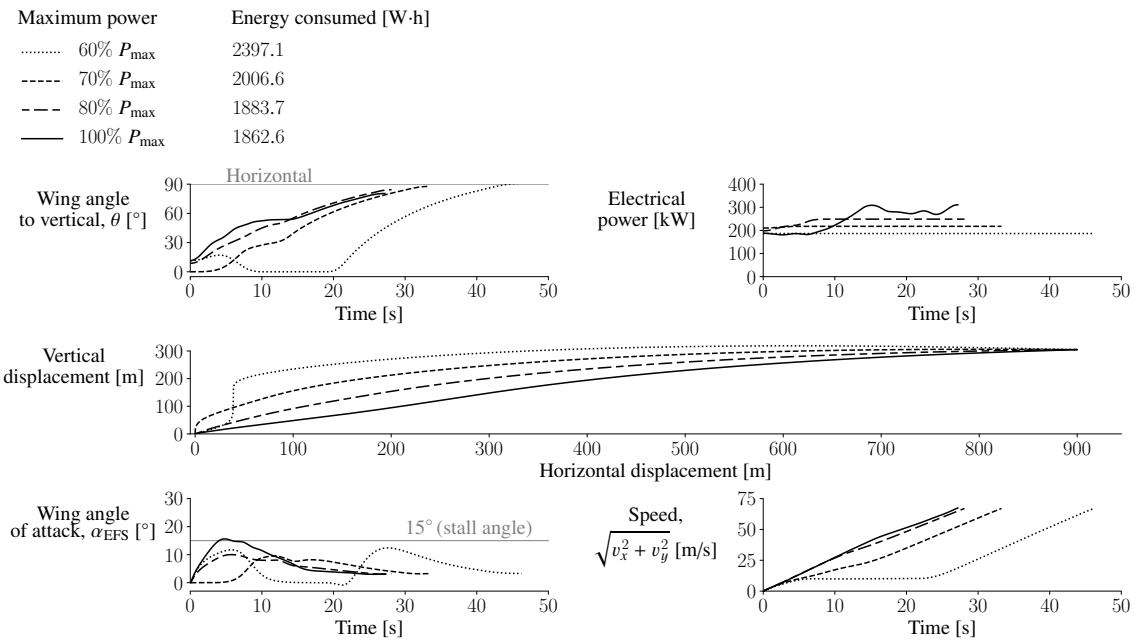

Figure 13: Results with varying maximum power for the optimization problem that includes the 0.3 g acceleration limit and the 900 m horizontal-displacement requirement (no stall constraints, $k_w = 100\%$)

Finally, keeping our observations so far in mind, we revisit the simplifications made in the modeling and discuss what differences may be expected if higher-order models are used in future work. Due to the challenges inherent in accurately predicting stall and post-stall behavior with tools such as panel-methods and RANS-based CFD [39–44], it is not obvious whether more accurate predictions can be obtained for the aerodynamics of the wings over a large range of angles of attack using these types of higher-order methods even with significant effort and computational cost. However, our results suggest that if such higher-order methods are used for the transition optimization of eVTOL configurations like the one studied here, it may be best to limit the wing-angle design variables such that the lift coefficients and angles of attack are restricted to pre-stall values. Since we found that the energy benefits in stalling the wings are practically negligible for an optimal takeoff, and considering real-world concerns such as safety, stability, and comfort, the effort required to address the accuracy and numerical challenges related to these higher-order methods near and beyond stall does not seem worthwhile for trajectory optimization.

For the propellers, methods such as blade-element methods (or more advanced methods such as free-wake methods [54, 63, 64]) can provide more accurate thrust and energy estimates than momentum theory. Connecting blade-element methods with panel-methods or RANS-based CFD tools are approaches that can help provide more accurate flow augmentation and propeller-wing interaction modeling [27, 51–53, 65, 66]. However, these approaches can have limitations related to inflow conditions when the propeller incidence angle is not small. Based on our results, improvements in propeller

modeling will likely impact the details of the optimal trajectory, but it seems unlikely that a significant impact will be made on the general shapes of the optimal climb profiles and the conclusions made on the effects of propeller-wing flow interaction, wing loading, and power-to-weight ratio on the electrical energy consumption.

Two major assumptions made in this work are that there is no interaction between the forward and rear wings (except for the interaction considered to calculate the effective span efficiencies), and that the wings rotate and behave identically. Reducing these simplifications and considering factors such as downwash, upwash, trim, and stability, the flows experienced by the forward and rear wings will not be identical. Depending on the modeling approach used, higher-order methods and separate control variables for the wings will help provide more accurate simulations. However, we do not expect the main trends seen in our optimization results to change significantly.

5 Conclusion

In this work, to address the lack of literature on the optimal takeoff trajectory for passenger tilt-wing eVTOL aircraft, we constructed a simplified model for a tandem tilt-wing eVTOL aircraft and numerically optimized its takeoff-to-cruise trajectory with the objective of minimizing energy consumption. We used low-order first-principles-based models for the aerodynamics, propulsion, propeller-wing flow-interaction, and flight-mechanics disciplines to capture the primary multidisciplinary trends. We carried out optimizations with and without stall and acceleration constraints, and with varying levels of flow augmentation from propellers.

The optimized trajectories without acceleration constraints involve first transitioning to forward flight and accelerating, followed by climbing at roughly constant speed, and then finally accelerating to the required cruise speed, all performed at or almost at maximum power. Without an acceleration constraint, the accelerations reach $1\,g$ in magnitude. With an acceleration limit of $0.3\,g$ for passenger comfort, the transition, climb, and acceleration phases are more gradual and less distinct, and are not carried out at maximum power.

The optimized takeoffs involve stalling the wings or flying near the stall angle of attack, both with and without the acceleration limit of $0.3\,g$. However, based on the optimization cases with stall constraints, we found that the energy penalty for avoiding stall is practically negligible.

With different levels of flow augmentation from the propellers, we found that the optimized trajectories have practically negligible differences in energy consumption. However, with the acceleration constraint, the optimized trajectories have noticeable differences in shape with the different levels of flow augmentation. With lower levels of flow augmentation, the optimized trajectories involve taking off with smaller wing angles to the vertical and gaining more altitude during the initial takeoff phase.

Based on our models, the optimized takeoff-to-cruise flight with the acceleration constraint, for the particular air-taxi mission requirements considered (cruise at a speed of 67 m/s and an altitude of 305 m), consumes 1.9 kWh of electrical energy (19 kg of installed-battery mass based on an installed-battery specific energy of 100 Wh/kg).

Without acceleration constraints, the optimized trajectories require 9% less electrical energy. Compared to a simpler and primarily hand-tuned trajectory in which the aircraft takes off, climbs at the wing angle for best rate of climb, and then accelerates to the required cruise speed, the optimized trajectories with the acceleration constraint require 5% less electrical energy.

We also studied the impact of changing the wing loading on the optimization results. With higher wing loadings (up to 250% of the baseline), we found that the optimized trajectories involve larger angles of attack, but the flight time and electrical energy consumed do not change substantially. We also found that, even with low levels of flow augmentation, it is still possible to avoid stalling the wings with this range of wing sizes.

Similarly, we studied the impact of decreasing the power-to-weight ratio and found that with low available power, the optimized takeoffs are carried out at or close to maximum power. The time and electrical energy required also increase as the maximum power available decreases. With the two lowest maximum-power levels considered (corresponding to maximum thrust-to-weight ratios at hover of 1.2 and 1.3), the optimized trajectories include purely vertical-flight phases, something not seen in the other optimization results presented in this paper. We also found that with low available power and low levels of flow augmentation, stalling the wings during takeoff can be unavoidable.

Overall, we conclude that the design space for the takeoff-to-cruise trajectory of the tilt-wing eVTOL aircraft that we study, with the mission specifications used in this work, is relatively flat from an energy consumption point of view. Relatively large changes to the flight profiles and the flow augmentation levels, as well as to the baseline wing loading and power-to-weight ratio, result in relatively small changes to the electrical energy consumed.

Readers are invited to experiment with the publicly available scripts linked to in this paper and study how the results and conclusions change for different specifications (e.g., different cruise altitude and speed requirements).

A Appendix: Comparison of the Tangler–Ostowari model with experimental data

Figures 14 and 15 show comparisons of the Tangler–Ostowari model described in Section 2.1 to experimental data from Ostowari and Naik [32] for rectangular NACA 4415 and NACA 4412 wings. Experimental data for two aspect ratios, 6 and 9, and two Reynolds numbers, 0.25 million and 1 million, are included for comparison. The Tangler–Ostowari model provides a reasonable model for the post-stall behavior and one of the limitations is that the post-stall drop in lift is not as sharp as seen in the experimental data.

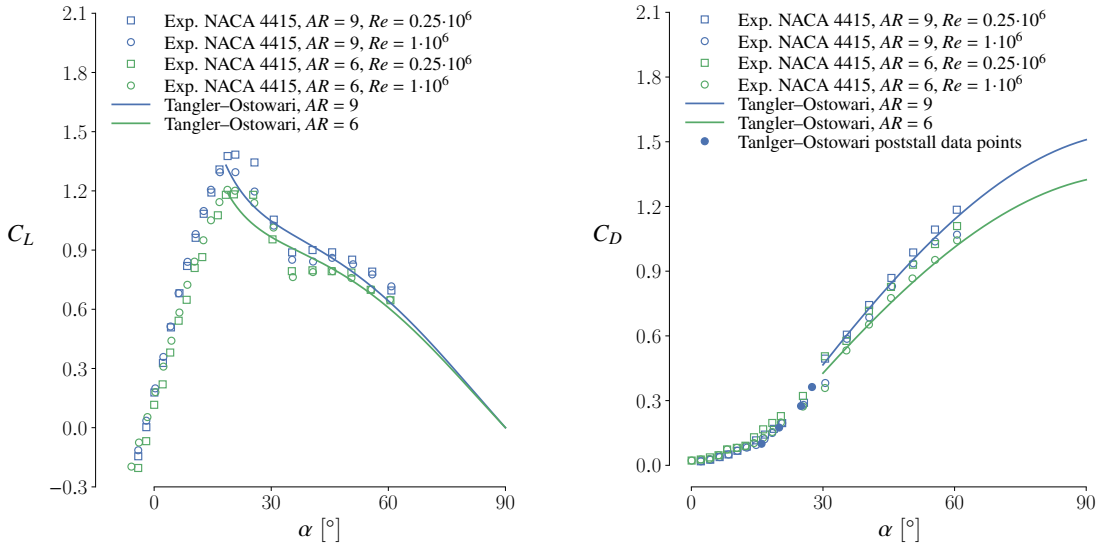

(a) Lift coefficient

(b) Drag coefficient

Figure 14: Post-stall coefficients of lift and drag from the Tangler–Ostowari model compared to experimental data from Ostowari and Naik [32] for rectangular NACA 4415 wings

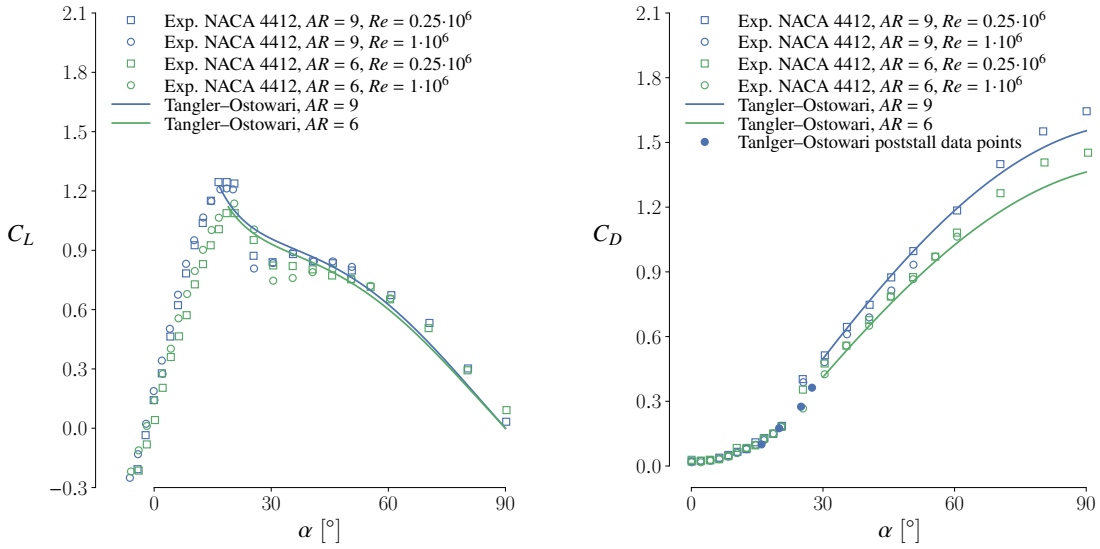

(a) Lift coefficient

(b) Drag coefficient

Figure 15: Post-stall coefficients of lift and drag from the Tangler–Ostowari model compared to experimental data from Ostowari and Naik [32] for rectangular NACA 4412 wings

B Appendix: Drag coefficient curve-fit for angles below 27.5°

Table 5 lists the pre-stall data points for the least-squares curve-fit used for computing the drag coefficient of each wing as a function of angle of attack for angles below 27.5°. Figure 16 shows the curve and data points for this least-squares curve-fit. The post-stall data points are listed in Table 1.

Table 5: Pre-stall drag coefficient data points used for the quartic curve-fit ($AR = 8$)

α	c_{d} [34]	$C_{\mathrm{D,induced}}$	$C_{\mathrm{D}} = c_{\mathrm{d}} + C_{\mathrm{D,induced}}$
0°	0.006	0.0	0.006
2°	0.0062	0.00137	0.00757
4°	0.007	0.00549	0.01249
6°	0.008	0.01234	0.02034
8°	0.0095	0.02194	0.03144
10°	0.012	0.03429	0.04629
12°	0.015	0.04937	0.06437

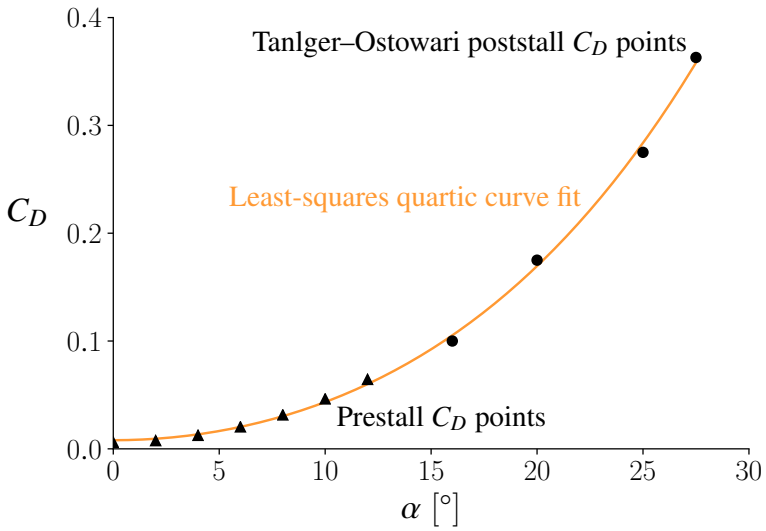

Figure 16: Least-squares quartic curve-fit for the wing drag coefficient for angles of attack below than 27.5°

C Appendix: Zoom-in of the initial phase of the optimized trajectories without acceleration constraints or horizontal-displacement requirements

Figure 17 provides a closer view of the initial transition phase of the trajectories shown in Figs. 5 and 6.

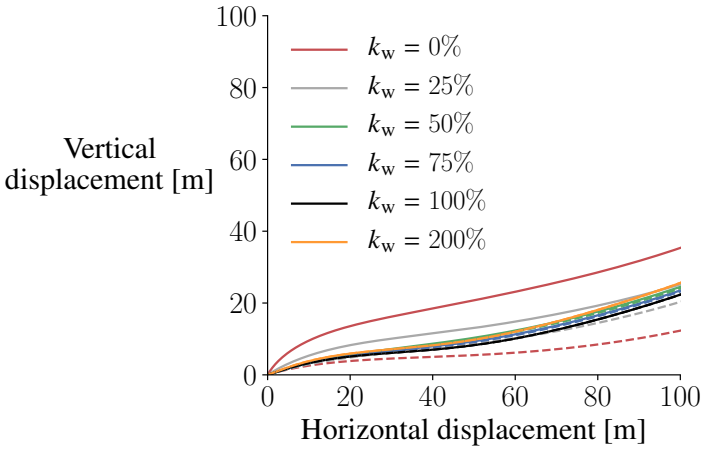

Figure 17: Zoomed-in transition phase of the trajectories shown in Figs. 5 and 6. The dashed curves correspond to the results without stall constraints.

D Appendix: Plots showing comparisons with varying numbers of B-spline control points

Figures 18 and 19 show comparisons of optimization results with varying numbers of B-spline control points for the wing-angle and electrical-power design variables.

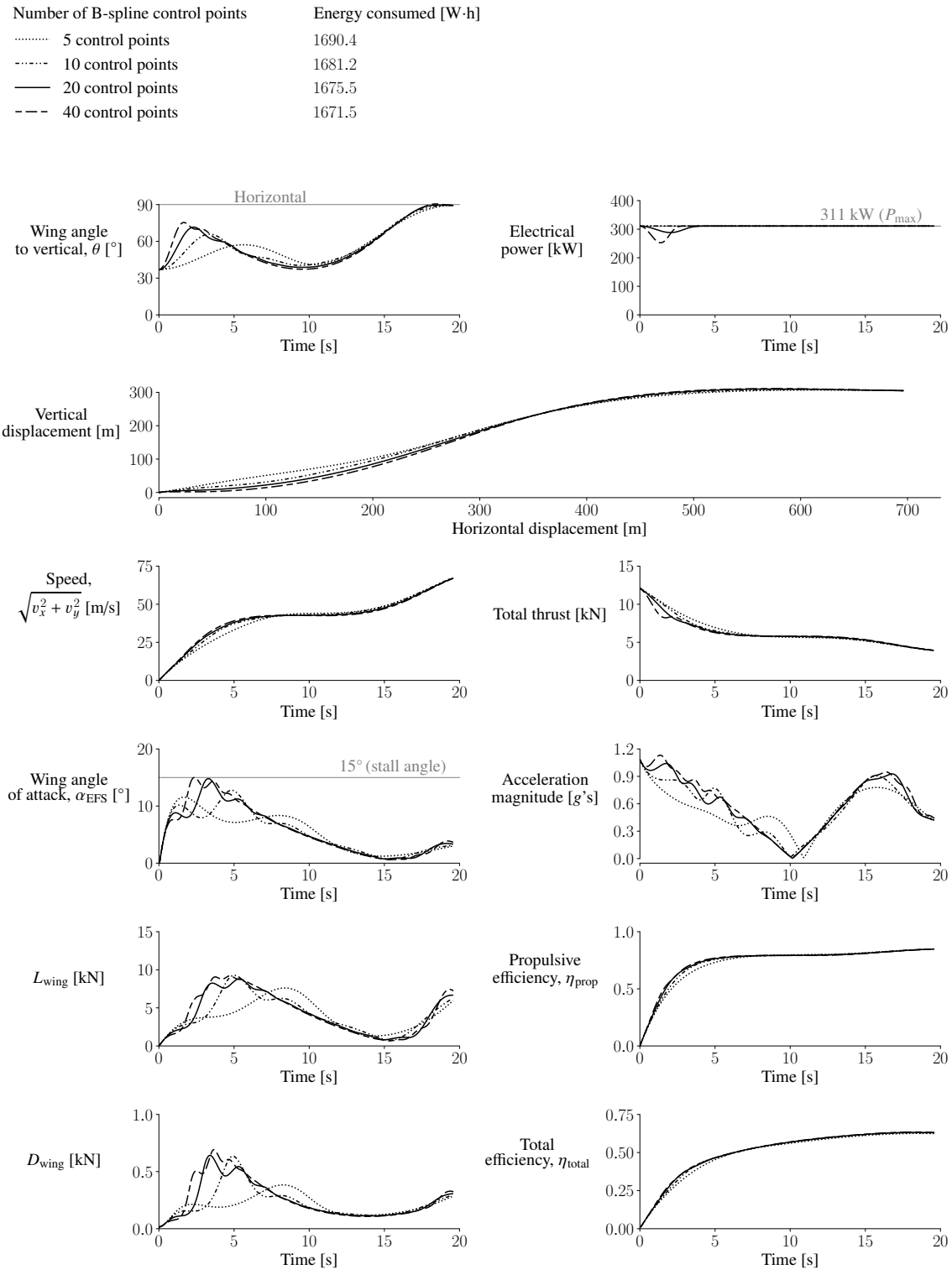

Figure 18: Optimization results for varying numbers of B-spline control points for the design variables, without stall or acceleration constraints ($k_{\mathrm{w}} = 100\%$, final horizontal displacements = 696 m)

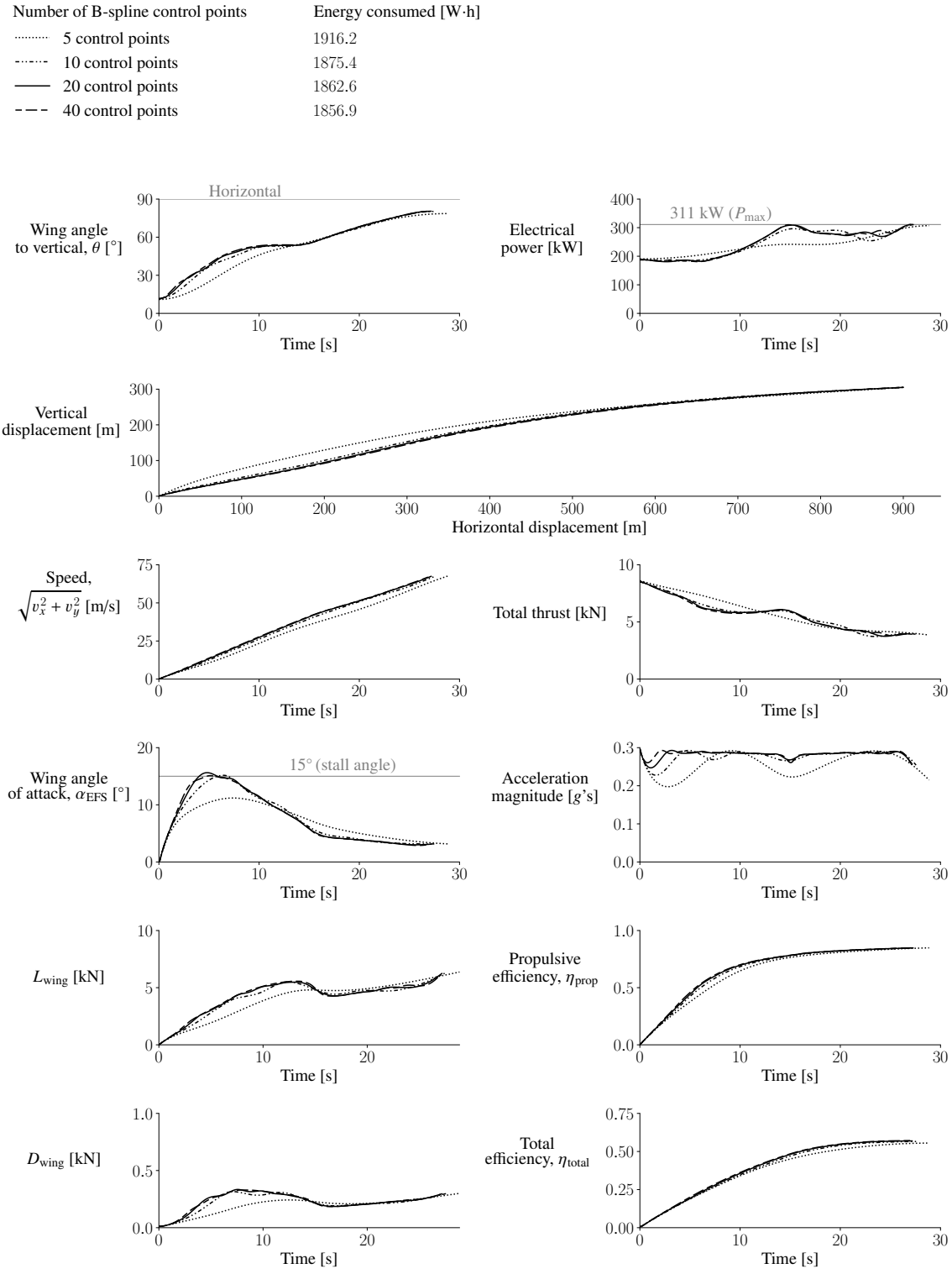

Figure 19: Optimization results for varying numbers of B-spline control points for the design variables, with the acceleration constraint and horizontal-displacement requirement (no stall constraints, $k_{\mathrm{w}} = 100\%$)

E Appendix: Energy values for optimizations without acceleration constraints but with the 900 m horizontal-displacement requirement

For a direct comparison to energy consumption values with the acceleration constraint and the horizontal-displacement requirement presented in Section 4.2, energy consumption values are listed in Table 6 for optimization cases without the acceleration constraint but with the horizontal-displacement requirement of 900 m.

Table 6: Energy consumption values for optimizations without acceleration constraints but with the 900 m horizontal-displacement requirement

k_w	Energy consumption without stall constraints [Wh]	Energy consumption with stall constraints [Wh]
0%	1694.3	1720.0
25%	1693.8	1707.1
50%	1694.9	1698.1
75%	1697.5	1697.5
100%	1700.2	1700.2
200%	1710.6	1710.6

Acknowledgments

We would like to thank Benjamin Brelje, John Jasa, and the anonymous reviewers for their valuable suggestions.

References

[1] Johnson, W., Silva, C., and Solis, E., "Concept Vehicles for VTOL Air Taxi Operations," *Proceedings of the AHS technical conference on Aeromechanics Design for Transformative Vertical Flight*, 2018.

[2] Pegg, R. J., "Summary of Flight-Test Results of the VZ-2 Tilt-Wing Aircraft," Technical Note NASA-TN-D-989, NASA, February 1962.

[3] "Development of the U.S. Army VZ 2 (Boeing Vertol-76) Research Aircraft," Technical Report R-219, The Boeing Company, August 1963.

[4] Konrad, J. W., "Flight and operational suitability testing of the XC-142, V/STOL assault transport," *AIAA Flight Test, Simulation and Support Conference*, AIAA, 1967. doi:10.2514/6.1967-261, AIAA-1967-261.

[5] Kelley, H. L., Reeder, J. P., and Champine, R. A., "Summary of a flight-test evaluation of the CL-84 tilt-wing V/STOL aircraft," Technical Memorandum NASA-TM-X-1914, NASA, March 1970.

[6] Nichols, J., "The Hiller X-18 Experimental Aircraft - Lessons Learned," *AIAA/AHS/ASEE Aircraft Design, Systems and Operations Conference*, AIAA, 1990. doi:10.2514/6.1990-3203, AIAA-90-3203.

[7] Phillips, F. C., "The Canadair CL-84 Experimental Aircraft - Lessons Learned," *AIAA/AHS/ASEE Aircraft Design, Systems and Operations Conference*, AIAA, 1990. doi:10.2514/6.1990-3205, AIAA-90-3205.

[8] Chana, W. F., and Sullivan, T. M., "The Tilt Wing Configuration for High Speed VSTOL Aircraft," *19th Congress of the International Council of the Aeronautical Sciences*, ICAS/AIAA, 1994.

[9] Kuhn, R. E., and Draper, J. W., "Investigation of the Aerodynamic Characteristics of a Model Wing-Propeller Combination and of the Wing and Propeller Separately at Angles of Attack up to 90°," Technical Report NACA-TR-1263, NASA, January 1956.

[10] Hargraves, C. R., "An analytical study of the longitudinal dynamics of a tilt-wing VTOL," Technical Report 561, U.S. Army Transportation Research Command, June 1961.

[11] Fay, C. B., "A Cursory Analysis Of The VTOL Tilt-Wing Performance And Control Problems," *Annals of the New York Academy of Sciences*, Vol. 107, No. 1, 1963, pp. 102–146. doi:10.1111/j.1749-6632.1963.tb13275.x.

[12] McKinney, M. O., Kirby, R. H., and Newsom, W. A., "Aerodynamic Factors To Be Considered In The Design Of Tilt-Wing V/STOL Airplanes," *Annals of the New York Academy of Sciences*, Vol. 107, No. 1, 1963, pp. 221–248. doi:10.1111/j.1749-6632.1963.tb13279.x.

[13] McCormick, B. W., *Aerodynamics of V/STOL Flight*, Academic Press, 1967.

[14] Chambers, J. R., and Grafton, S. B., "Calculation of the dynamic longitudinal stability of a tilt-wing V/STOL aircraft and correlation with model flight tests," Technical Note NASA-TN-D-4344, NASA, February 1968.

[15] Holsten, J., Ostermann, T., and Moormann, D., "Design and wind tunnel tests of a tiltwing UAV," *CEAS Aeronautical Journal*, Vol. 2, No. 1, 2011, pp. 69–79. doi:10.1007/s13272-011-0026-4.

[16] Cetinsoy, E., Dikyar, S., Hancer, C., Oner, K., Sirimoglu, E., Unel, M., and Aksit, M., "Design and construction of a novel quad tilt-wing UAV," *Mechatronics*, Vol. 22, No. 6, 2012, pp. 723–745. doi:10.1016/j.mechatronics.2012.03.003.

[17] Sato, M., and Muraoka, K., "Flight Controller Design and Demonstration of Quad-Tilt-Wing Unmanned Aerial Vehicle," *Journal of Guidance, Control, and Dynamics*, Vol. 38, No. 6, 2015, pp. 1071–1082. doi:10.2514/1.G000263.

[18] Hartmann, P., Meyer, C., and Moormann, D., "Unified Velocity Control and Flight State Transition of Unmanned Tilt-Wing Aircraft," *Journal of Guidance, Control, and Dynamics*, Vol. 40, No. 6, 2017, pp. 1348–1359. doi:10.2514/1.G002168.

[19] Fredericks, W. J., McSwain, R. G., Beaton, B. F., Klassman, D. W., and Theodore, C. R., "Greased Lightning (GL-10) Flight Testing Campaign," Technical Memorandum NASA-TM-2017-219643, NASA, July 2017.

[20] Stone, R. H., and Clarke, G., "Optimization of Transition Maneuvers for a Tail-Sitter Unmanned Air Vehicle," *Australian Aerospace International Congress, Paper 105*, 2001.

[21] Stone, R. H., Anderson, P., Hutchison, C., Tsai, A., Gibbens, P., and Wong, K. C., "Flight Testing of the T-Wing Tail-Sitter Unmanned Air Vehicle," *Journal of Aircraft*, Vol. 45, No. 2, 2008, pp. 673–685. doi:10.2514/1.32750.

[22] Kubo, D., and Suzuki, S., "Tail-Sitter Vertical Takeoff and Landing Unmanned Aerial Vehicle: Transitional Flight Analysis," *Journal of Aircraft*, Vol. 45, No. 1, 2008, pp. 292–297. doi:10.2514/1.30122.

[23] Maqsood, A., and Go, T. H., "Optimization of transition maneuvers through aerodynamic vectoring," *Aerospace Science and Technology*, Vol. 23, No. 1, 2012, pp. 363–371. doi:10.1016/j.ast.2011.09.004.

[24] Oosedo, A., Abiko, S., Konno, A., and Uchiyama, M., "Optimal transition from hovering to level-flight of a quadrotor tail-sitter UAV," *Autonomous Robots*, Vol. 41, No. 5, 2017, pp. 1143–1159. doi:10.1007/s10514-016-9599-4.

[25] Pradeep, P., and Wei, P., "Energy Optimal Speed Profile for Arrival of Tandem Tilt-Wing eVTOL Aircraft with RTA Constraint," *Proceedings of IEEE/CSAA Guidance, Navigation and Control Conference (GNCC), Xiamen, China*, 2018.

[26] Verling, S., Stastny, T., Battig, G., Alexis, K., and Siegwart, R., "Model-based transition optimization for a VTOL tailsitter," *2017 IEEE International Conference on Robotics and Automation (ICRA)*, IEEE, 2017. doi:10.1109/icra.2017.7989454.

[27] Stone, R. H., "Aerodynamic Modeling of the Wing-Propeller Interaction for a Tail-Sitter Unmanned Air Vehicle," *Journal of Aircraft*, Vol. 45, No. 1, 2008, pp. 198–210. doi:10.2514/1.15705.

[28] Gray, J. S., Hwang, J. T., Martins, J. R. R. A., Moore, K. T., and Naylor, B. A., "OpenMDAO: An open-source framework for multidisciplinary design, analysis, and optimization," *Structural and Multidisciplinary Optimization*, Vol. 59, No. 4, 2019, pp. 1075–1104. doi:10.1007/s00158-019-02211-z.

[29] Hwang, J. T., and Martins, J. R. R. A., "A computational architecture for coupling heterogeneous numerical models and computing coupled derivatives," *ACM Transactions on Mathematical Software*, Vol. 44, No. 4, 2018, p. Article 37. doi:10.1145/3182393.

[30] Tangler, J. L., and Ostowari, C., "Horizontal axis wind turbine post stall airfoil characteristics synthesization," Conference paper presented at the DOE/NASA Wind Turbine Technology Workshop, May 1984. In Collected Papers on Wind Turbine Technology, NASA-CR-195432, May 1995.

[31] Viterna, L. A., and Corrigan, R. D., "Fixed pitch rotor performance of large horizontal axis wind turbines," *Large Horizontal-Axis Wind Turbines (NASA-CP-2230)*, NASA Conference Publication, 1982, pp. 69–86.

[32] Ostowari, C., and Naik, D., "Post-Stall Wind Tunnel Data for NACA 44XX Series Airfoil Sections," Subcontract Report SERI/STR-217-2559, Solar Energy Research Institute, January 1985.

[33] Critzos, C. C., Heyson, H. H., and Boswinkle Jr., R. W., "Aerodynamic characteristics of NACA 0012 airfoil section at angles of attack from 0 degrees to 180 degrees," Technical Note NACA-TN-3361, NACA, January 1955.

[34] Abbott, I. H., and Von Doenhoff, A. E., *Theory of wing sections, including a summary of airfoil data*, Dover Publications, New York, 1959.

[35] Prandtl, L., "Induced drag of multiplanes," Technical Note NACA-TN-182, NACA, February 1924.

[36] McLaughlin, M. D., "Calculations, and Comparison with an Ideal Minimum, of Trimmed Drag for Conventional and Canard Configurations Having Various Levels of Static Stability," Technical Note NASA-TN-D-8391, NASA, May 1977.

[37] Kreisselmeier, G., and Steinhauser, R., "Systematic Control Design by Optimizing a Vector Performance Index," *International Federation of Active Controls Symposium on Computer-Aided Design of Control Systems, Zurich, Switzerland*, 1979. doi:10.1016/S1474-6670(17)65584-8.

[38] Winslow, J., Otsuka, H., Govindarajan, B., and Chopra, I., "Basic Understanding of Airfoil Characteristics at Low Reynolds Numbers ($10^4 - 10^5$)," *Journal of Aircraft*, Vol. 55, No. 3, 2018, pp. 1050–1061. doi:10.2514/1.c034415.

[39] van Dam, C. P., Kam, J. C. V., and Paris, J. K., "Design-Oriented High-Lift Methodology for General Aviation and Civil Transport Aircraft," *Journal of Aircraft*, Vol. 38, No. 6, 2001, pp. 1076–1084. doi:10.2514/2.2875.

[40] Rumsey, C. L., Allison, D. O., Biedron, R. T., Buning, P. G., Gainer, T. G., Morrison, J. H., Rivers, S. M., Mysko, S. J., and Witkowski, D. P., "CFD sensitivity analysis of a modern civil transport near buffet-onset conditions," Tech. Rep. TM-2001-211263, NASA, 2001.

[41] van Dam, C., "The aerodynamic design of multi-element high-lift systems for transport airplanes," *Progress in Aerospace Sciences*, Vol. 38, No. 2, 2002, pp. 101–144. doi:10.1016/s0376-0421(02)00002-7.

[42] Mukherjee, R., and Gopalarathnam, A., "Poststall Prediction of Multiple-Lifting-Surface Configurations Using a Decambering Approach," *Journal of Aircraft*, Vol. 43, No. 3, 2006, pp. 660–668. doi:10.2514/1.15149.

[43] Petrilli, J. L., Paul, R. C., Gopalarathnam, A., and Frink, N. T., "A CFD Database for Airfoils and Wings at Post-Stall Angles of Attack," *31st AIAA Applied Aerodynamics Conference*, AIAA, 2013. doi:10.2514/6.2013-2916, AIAA-2013-2916.

[44] Parenteau, M., Sermeus, K., and Laurendeau, E., "VLM Coupled with 2.5D RANS Sectional Data for High-Lift Design," *2018 AIAA Aerospace Sciences Meeting*, AIAA, 2018. doi:10.2514/6.2018-1049, AIAA-2018-1049.

[45] Glauert, H., "A General Theory of the Autogyro," Reports and Memoranda 1111, Aeronautical Research Committee, 1926.

[46] de Young, J., "Propeller at high incidence," *Journal of Aircraft*, Vol. 2, No. 3, 1965, pp. 241–250. doi:10.2514/3.43646.

[47] Leishman, J. G., *Principles of Helicopter Aerodynamics*, The Press Syndicate of the University of Cambridge, 2000.

[48] Selig, M., "Modeling Full-Envelope Aerodynamics of Small UAVs in Realtime," *AIAA Atmospheric Flight Mechanics Conference*, AIAA, 2010. doi:10.2514/6.2010-7635, AIAA-2010-7635.

[49] Patterson, M. D., "Conceptual Design of High-Lift Propeller Systems for Small Electric Aircraft," Ph.D. thesis, Georgia Institute of Technology, 2016. URL `http://hdl.handle.net/1853/55569`.

[50] Patterson, M. D., Derlaga, J. M., and Borer, N. K., "High-Lift Propeller System Configuration Selection for NASA's SCEPTOR Distributed Electric Propulsion Flight Demonstrator," *16th AIAA Aviation Technology, Integration, and Operations Conference*, AIAA, 2016. doi:10.2514/6.2016-3922, AIAA-2016-3922.

[51] Deere, K. A., Viken, S. A., Carter, M. B., Viken, J. K., Derlaga, J. M., and Stoll, A. M., "Comparison of High-Fidelity Computational Tools for Wing Design of a Distributed Electric Propulsion Aircraft," *35th AIAA Applied Aerodynamics Conference*, AIAA, 2017. doi:10.2514/6.2017-3925, AIAA-2017-3925.

[52] Alba, C., Elham, A., German, B. J., and Veldhuis, L. L., "A surrogate-based multi-disciplinary design optimization framework modeling wing-propeller interaction," *Aerospace Science and Technology*, Vol. 78, 2018, pp. 721–733. doi:10.1016/j.ast.2018.05.002.

[53] Stokkermans, T. C. A., van Arnhem, N., Sinnige, T., and Veldhuis, L. L. M., "Validation and Comparison of RANS Propeller Modeling Methods for Tip-Mounted Applications," *AIAA Journal*, Vol. 57, No. 2, 2019, pp. 566–580. doi:10.2514/1.J057398.

[54] Cole, J. A., Maughmer, M. D., Kinzel, M., and Bramesfeld, G., "Higher-Order Free-Wake Method for Propeller–Wing Systems," *Journal of Aircraft*, Vol. 56, No. 1, 2019, pp. 150–165. doi:10.2514/1.c034720.

[55] Selig, M. S., "Real-Time Flight Simulation of Highly Maneuverable Unmanned Aerial Vehicles," *Journal of Aircraft*, Vol. 51, No. 6, 2014, pp. 1705–1725. doi:10.2514/1.c032370.

[56] Poon, N. M. K., and Martins, J. R. R. A., "An Adaptive Approach to Constraint Aggregation Using Adjoint Sensitivity Analysis," *Structural and Multidisciplinary Optimization*, Vol. 34, No. 1, 2007, pp. 61–73. doi:10.1007/s00158-006-0061-7.

[57] Lambe, A. B., Martins, J. R. R. A., and Kennedy, G. J., "An Evaluation of Constraint Aggregation Strategies for Wing Box Mass Minimization," *Structural and Multidisciplinary Optimization*, Vol. 55, No. 1, 2017, pp. 257–277. doi:10.1007/s00158-016-1495-1.

[58] Gill, P. E., Murray, W., and Saunders, M. A., "SNOPT: An SQP Algorithm for Large-Scale Constrained Optimization," *SIAM Review*, Vol. 47, No. 1, 2005, pp. 99–131. doi:10.1137/S0036144504446096.

[59] Martins, J. R. R. A., Sturdza, P., and Alonso, J. J., "The Complex-Step Derivative Approximation," *ACM Transactions on Mathematical Software*, Vol. 29, No. 3, 2003, pp. 245–262. doi:10.1145/838250.838251.

[60] Hargraves, C. R., and Paris, S. W., "Direct trajectory optimization using nonlinear programming and collocation," *Journal of Guidance, Control, and Dynamics*, Vol. 10, No. 4, 1987, pp. 338–342. doi:10.2514/3.20223.

[61] Hendricks, E. S., Falck, R. D., and Gray, J. S., "Simultaneous Propulsion System and Trajectory Optimization," *18th AIAA/ISSMO Multidisciplinary Analysis and Optimization Conference*, Denver, CO, 2017. doi:10.2514/6.2017-4435, AIAA-2017-4435.

[62] Gebhard, J. W., "Acceleration and Comfort in Public Ground Transportation," Transportation Programs Report TPR 002, The Johns Hopkins University, 1970.

[63] Bramesfeld, G., and Maughmer, M. D., "Relaxed-Wake Vortex-Lattice Method Using Distributed Vorticity Elements," *Journal of Aircraft*, Vol. 45, No. 2, 2008, pp. 560–568. doi:10.2514/1.31665.

[64] Patterson, M. D., and German, B., "Conceptual Design of Electric Aircraft with Distributed Propellers: Multidisciplinary Analysis Needs and Aerodynamic Modeling Development," *52nd Aerospace Sciences Meeting*, AIAA, 2014. doi:10.2514/6.2014-0534, AIAA-2014-0534.

[65] Stoll, A. M., Bevirt, J., Moore, M. D., Fredericks, W. J., and Borer, N. K., "Drag Reduction Through Distributed Electric Propulsion," *14th AIAA Aviation Technology, Integration, and Operations Conference*, AIAA, 2014. doi:10.2514/6.2014-2851, AIAA-2014-2851.

[66] Hwang, J. T., and Ning, A., "Large-scale multidisciplinary optimization of an electric aircraft for on-demand mobility," *2018 AIAA/ASCE/AHS/ASC Structures, Structural Dynamics, and Materials Conference*, Kissimmee, FL, 2018. doi:10.2514/6.2018-1384, AIAA-2018-1384.